

Master's Thesis

---

**Advancing Forest Radiative Transfer  
Modeling: TLS-Derived Explicit  
Geometries in DART**

---

Patrick McClatchy

Supervisor: Dr. Julian Frey  
2nd Examiner: Prof. Dr. Teja Kattenborn

Albert-Ludwigs-University Freiburg  
Faculty of Environment and Natural Resources  
Forest Growth and Dendroecology  
Juli 01<sup>st</sup>, 2024

**Writing period**

01.01.2024 – 01.07.2024

**Supervisors**

Dr. Julian Frey, Prof. Dr. Teja Kattenborn

Albert-Ludwigs-University Freiburg

Faculty of Environment and Natural Resources Forest Growth and Dendroecology

# Abstract

Light availability and distribution are critical factors in forest ecosystems, driving processes such as species competition, ecosystem functioning, productivity, and diversity. Due to the shortcomings and challenges of direct and indirect measures of light conditions, radiative transfer models (RTMs) aim to provide accurate, high-resolution solutions to quantify light conditions within forest ecosystems. As canopy structure significantly influences light variability, accurately representing foliage and wood structures within RTMs is crucial.

This thesis presents a workflow for parameterizing the Discrete Anisotropic Radiative Transfer Model (DART) using explicit geometries reconstructed from terrestrial laser scans of a single apple tree (*Malus domestica* Borkh.) and simulating photosynthetically active radiation (PAR) (400-700 nm) underneath and around the tree. The simulation was validated against PAR measurements collected using 60 quantum sensors and compared to a voxel-based method at two voxel sizes (0.2 m and 1 m) to quantify differences in simulation accuracy and computational efficiency.

The simulated values were highly correlated with the measured PAR values ( $r = 0.89$ ), outperforming the voxel-based approaches in both accuracy and computation time. However, some sensors failed to accurately represent diurnal PAR dynamics and exhibited overestimated PAR values in shaded areas, suggesting the need for species-specific optical properties and improved atmospheric parameterization. The findings underscore the potential of integrating TLS data with radiative transfer models to enhance our understanding of light dynamics in forest ecosystems, providing valuable insights for research and management. Future research should validate this methodology across diverse forest types to enhance its robustness. Further development of the 3D reconstruction process by including dynamic variables representing the effects of environmental conditions, growth and phenology should improve simulation accuracy. The presented approach effectively simulates light extinction through the canopy, offering detailed insights into micro-structural light patterns and proving potential for large-scale applications.

# Contents

<b>1</b>	<b>Introduction</b>	<b>9</b>
1.1	Quantifying Light Distribution In Forest Ecosystems . . . . .	10
1.1.1	In-situ measurements . . . . .	10
1.1.2	Radiative Transfer Models . . . . .	13
1.2	Research Objective . . . . .	19
<b>2</b>	<b>Materials and Methods</b>	<b>20</b>
2.1	Study Site . . . . .	20
2.2	PAR Measurements . . . . .	22
2.3	LIDAR Data . . . . .	22
2.4	Stem and Foliage Model Construction . . . . .	23
2.5	Voxelization . . . . .	25
2.6	DART Parametrisation . . . . .	25
2.7	Validation . . . . .	29
<b>3</b>	<b>Results</b>	<b>30</b>
3.1	TLS . . . . .	30
3.2	Voxelization and PAD . . . . .	31
3.3	Stem and Foliage Model Construction . . . . .	32
3.4	Simulated PAR vs. Measured PAR . . . . .	34
3.4.1	PAR measurements . . . . .	34
3.4.2	DART Simulations . . . . .	35
3.4.3	Validation . . . . .	37
3.5	Computational Efficiency . . . . .	40
<b>4</b>	<b>Discussion</b>	<b>42</b>
4.1	Simulation Accuracy . . . . .	42
4.2	Validation Data . . . . .	45
4.3	Comparison with Other Approaches . . . . .	45
4.4	Implications and Limitations . . . . .	47

4.5 Future Research . . . . .	49
<b>5 Conclusion</b>	<b>51</b>
<b>6 Acknowledgments</b>	<b>52</b>
Bibliography	53
<b>Appendix A</b>	<b>63</b>
<b>Appendix B</b>	<b>67</b>

# List of Figures

1	DART framework . . . . .	18
2	Study site location and target tree . . . . .	20
3	Methods Overview Diagram . . . . .	21
4	Experimental setup PAR sensors . . . . .	23
5	3D polygon constructions . . . . .	24
6	DART coordinate system . . . . .	26
7	DART framework . . . . .	27
8	Simulated PAR sensors . . . . .	28
9	Overview Point Cloud Target Tree . . . . .	30
10	Voxelized Plant Area Density (PAD) distribution . . . . .	31
11	3D representation of the target tree . . . . .	32
12	Screenshot of the DART 3D viewer showing the scene with the explicit geometry tree model and white Lambertian surfaces as used PAR sensor targets (grey circles). . . . .	33
13	Measured Radiation . . . . .	34
14	DART Nadir Sensor . . . . .	35
15	DART Nadir Sensor . . . . .	36
16	PAR Time Series . . . . .	38
17	Simulated vs. Measured PAR . . . . .	39
18	Confusion Matrices . . . . .	41
B1	Time series of measured and simulated PAR values for all three scene types. (Logger 1, Logger 2) . . . . .	68
B2	Time series of measured and simulated PAR values for all three scene types. (Logger 3, Logger 4) . . . . .	69
B3	Time series of measured and simulated PAR values for all three scene types. (Logger 5, Logger 6) . . . . .	70

# List of Tables

1	3D crown models . . . . .	14
2	Software Used in Methodology . . . . .	22
3	Correlation Coefficients . . . . .	39
A1	Per-sensor Pearson's correlation coefficient $r$ for measured vs simulated values (Logger 1 and 2) . . . . .	64
A2	Per-sensor Pearson's correlation coefficient $r$ for measured vs simulated values (Logger 3 and 4) . . . . .	65
A3	Per-sensor Pearson's correlation coefficient $r$ for measured vs simulated values (Logger 5 and 6) . . . . .	66

# List of Abbreviations

<b>BOA</b>	Bottom of Atmosphere
<b>DART</b>	Discrete Anisotropic Radiative Transfer
<b>DEM</b>	Digital Elevation Model
<b>DWD</b>	German Weather Service
<b>GNSS</b>	Global Navigation Satellite System
<b>LAI</b>	Leaf Area Index
<b>LOP</b>	Leaf Optical Properties
<b>MODTRAN</b>	MODerate resolution atmospheric TRANsmission
<b>PAD</b>	Plant Area Density
<b>PAR</b>	Photosynthetically Active Radiation
<b>PPFD</b>	Photosynthetic Photon Flux Density
<b>QSM</b>	Quantitative Structure Models
<b>RAMI</b>	Radiative Transfer Model Intercomparison
<b>RTM</b>	Radiative Transfer Model
<b>TLS</b>	Terrestrial Laser Scanning

# 1 Introduction

Light availability is a key environmental factor in forest ecosystems, determining essential biological and ecological processes such as photosynthesis, evapotranspiration, respiration, and phenology (Sage and Kubien, 2007; Kull and Kruijt, 1998; Canham et al., 1990; Van der Zande et al., 2010; Caffarra and Donnelly, 2011). Consequently, the light distribution in forest ecosystems, both within and beneath the forest canopy, affects tree regeneration, growth, survival and competition as well as the productivity, diversity and composition of the under-story vegetation (De Pauw et al., 2022; Leuchner et al., 2012). Hence, the dynamics of solar radiation within the canopy extensively shapes the structure and overall composition of forest communities and as a result also determines larger scale ecophysiological processes, for example, carbon, energy and nutrient fluxes (Millard, 1996; Restrepo-Coupe et al., 2013; Baldocchi et al., 2001).

An accurate quantification of the distribution of solar radiation within forest stands therefore greatly benefits the advancement of ecological and silvicultural research, by allowing for a more detailed understanding of physiological and ecological processes from a single-tree to ecosystem perspective. This can provide the basis for implementing informed forest management strategies, by for example optimizing stand density or species composition based on light availability assessments (Forrester et al., 2019). Precise information on solar radiation, specifically surface irradiance, further provides a basis for the calibration of vegetation indices retrieved by imaging spectroscopy such as the NDVI, derived from top of canopy reflectance (Ferreira et al., 2018; Wang et al., 2018). This enables the accurate remote sensing and interpretation of the traits and functioning of vegetated ecosystems.

However, in-situ measurements of light within forests presents challenges due to complex canopy structures and the fluctuations of sunlight across spatial, temporal, and seasonal scales (Niinemets, 2007; Valladares, 2003; Kükenbrink et al., 2021). Radiative transfer modeling (RTM) provides a valuable tool for addressing this issue by simulating the absorption, scattering, and reflection of light within forest canopies at varying complexity.

Over the last 40 years RTMs have evolved from simple empirical models to complex multi-layered approaches (Ligot et al., 2014), enhancing in precision and applicability. Combined with modern terrestrial laser scanning (TLS) based methods for assessing forest structure (Danson et al., 2018), new possibilities for simulating the dynamics of solar radiation in forest stands arise.

In the following, I will outline the state of knowledge regarding both in-situ measurement methods and RTM-based approaches to quantify the distribution of light within forest ecosystems. Based on this I will propose a method for parameterizing a RTM with TLS data of a single tree to simulate light extinction by the canopy.

## 1.1 Quantifying Light Distribution In Forest Ecosystems

### 1.1.1 In-situ measurements

In-situ methods for the quantification of light levels within forests can be separated into either direct or indirect, both with their own benefits and drawbacks. Direct methods measure light levels within the forest using tools like radiometers or quantum sensors. In contrast, indirect methods estimate light availability by inferring conditions from other parameters.

#### Direct methods

Early studies directly measuring light levels in forests typically used rudimentary photometric measures such as photographic emulsions or light meters with either selenium or silicon photocells. These photocells convert radiation into voltage for measurement (Ashton, 1958; Matusz, 1953). However, these early instruments often lacked precision and reliability, and their measurements were susceptible to environmental factors such as temperature and humidity. Further, these methods measure illuminance or brightness as perceived by the human eye (in lux or lumen) and there is no information on the spectral composition of the light being measured. The spectral response determining plant processes differs from these photometric measurements which therefore aren't directly suitable for estimating the effects on plant physiological functioning (Jennings et al., 1999).

Radiometric measurements evaluate the energy content of solar radiation in joules or watts, useful for investigating heat or water balances in forests. Instruments like pyranometers typically measure incoming shortwave radiation, often used as input for

energy balance models estimating snow cover or soil conditions (Webster et al., 2016; Gleason et al., 2013). Different types of radiometers provide integrated measurements over a specific range of wavelengths, depending on the specific use case. Two key concepts in radiometric measurements are irradiance and radiance. Irradiance is defined as the total amount of radiant energy received by a surface per unit area, typically measured in watts per square meter ( $\text{W}/\text{m}^2$ ). It represents an integral over all directions of the radiance hitting the surface. Radiance, on the other hand, is the amount of light that passes through or is emitted from a particular area and falls within a given solid angle in a specified direction. It is measured in watts per square meter per steradian ( $\text{W}/\text{m}^2/\text{sr}$ ).

Spectroradiometers can capture the full spectrum of light conditions, providing detailed measurements and the ability to quantify the differences in light extinction by the canopy at differing wavelengths (Kükenbrink et al., 2019). Despite their precision, spectroradiometers are often less favored in field studies due to their complexity and high financial costs, limiting the ability to measure at larger spatial and temporal scales.

Photosynthetically Active Radiation (PAR) represents the spectral range of light (400-700 nm) that plants use for photosynthesis. Measuring PAR distribution within a forest canopy is therefore essential for assessing the light environment, as it directly influences plant growth and ecosystem productivity. Although various studies have used radiometric measuring systems to quantify global, diffuse or reflected PAR (Ross and Sulev, 2000), more commonly quantum sensors are used, which are specifically developed and calibrated for accurately measuring PAR.

Quantum sensors measure light as photosynthetic photon flux density (PPFD) by counting the total number or flux of quanta per unit area, typically measured in micro-moles of photons. Currently, quantum sensors are commonly used to measure PAR as they are often cost-effective and portable, providing highly accurate and sensitive measurements (Jennings et al., 1999; Caya et al., 2018; Ross and Sulev, 2000; Parker et al., 2019).

Various studies outlined the inherent issues and challenges regarding direct measurements of radiation in forest environments (Ross and Sulev, 2000; Jennings et al., 1999). Due to the high structural complexity of forests (McElhinny et al., 2005), the light conditions vary strongly on both spatial (horizontally and vertically) and temporal scales from minutes to years (Niinemets, 2007; Valladares, 2003). Therefore, comprehensively quantifying PAR using direct measurements presents a large logistical and financial challenge, requiring large amounts of sensors and data loggers

and long time series, presenting an issue of keeping sensors clean and horizontal to avoid measurement inaccuracies (Jennings et al., 1999; Brown et al., 2000).

Previous research has addressed these challenges, proposing direct measurements to solely be used for the calibration and validation of indirect measurement techniques from which light conditions can be derived (Jennings et al., 1999; Ferment et al., 2001; Brown et al., 2000; Tinya et al., 2009).

### **Indirect methods**

Early indirect methods were mainly based on visual assessments and simple photographic techniques. A major leap forward occurred with the introduction of hemispherical photography by Anderson (1964). This technique uses fisheye lens photography of the forest canopy to determine the light environment underneath. Digital cameras have greatly simplified the process of image capture and further development enhanced the accuracy and efficiency of extracting canopy structure data from hemispherical photographs. Hemispherical photography quantifies the gap fraction, or the proportion of sky visible through the canopy, at various zenith angles. This method utilizes the Beer-Lambert law to relate gap fraction to parameters such as leaf area index (LAI) and canopy structure, assuming a uniform distribution of leaves, non-transmissive foliage, and a random leaf orientation. The Beer-Lambert law states that the amount of light absorbed by a medium increases with the medium's concentration and the distance the light travels through it, resulting in an exponential decrease of light availability through the canopy (Macfarlane et al., 2007; Frazer et al., 1999). Similarly, plant canopy analyzers such as the LAI-2200 (Danner et al., 2015) estimate the LAI at a specific position from which light conditions can be derived. Essentially, both methods assess the proportion of the sky that is obscured along a particular line of sight. Although widely used, these indirect measures have notable drawbacks. They are highly sensitive to overall lighting conditions. Optimal results are usually obtained under uniformly overcast skies to minimize shadows and variations which can lead to inaccurate results. Generally, the challenges of optical distortions, calibration issues and blurred or inconsistent images due to movement can make these methods impractical for obtaining accurate and high-resolution results. Hemispherical photography has also shown to be less sensitive to extensive temporal variations of PAR in the forest under-story than direct measurements (Jennings et al., 1999).

Further, these point-based measurements fail to represent spatial variability of light

conditions across a heterogeneous forest landscape and the need to cover large areas with multiple sampling points can be logistically challenging. In addition, capturing temporal variability poses a significant issue, as these indirect measuring methods cannot be left unattended in the field for extended periods (Tinya et al., 2009; Brown et al., 2000; Ferment et al., 2001; Jennings et al., 1999).

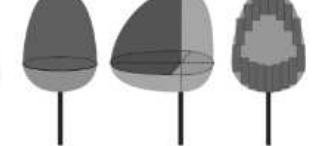
To address the limitations and challenges which both direct and indirect in-situ measures of light conditions present, various approaches of radiative transfer modeling (RTM) have been developed with the aim provide high-resolution results across both spatial and temporal scales.

### 1.1.2 Radiative Transfer Models

The elementary forms of radiative transfer schemes underlie the simple assumption of the exponential decrease of incoming light within the canopy. These models based on Beer's law of light extinction define the canopy as a uniformly horizontally distributed turbid layer (de León and Bailey, 2019). Although prevalent in various land surface models (Kükenbrink et al., 2021), this assumption has only shown an acceptable accuracy for dense and uniform forest stands (Hale et al., 2009; Da Silva et al., 2012), neglecting diffuse irradiance and horizontal and vertical heterogeneity. Two-stream models were developed to address this by dividing radiation into upward and downward streams as well as diffuse and direct radiation, for example, applied by Jogireddy et al. (2006). These simplistic representations of the extinction of light within forest overlook the significant effect of canopy structure on light availability (Niinemets, 2007; McElhinny et al., 2005).

Therefore, numerous approaches have been developed to represent forest structures in varying complexity and resolution. Early canopy modeling approaches developed simplified representations with conical or oval crown shapes, like the geometric-optical model by Li and Strahler (1985). Here key parameters are defined, including tree density, height distribution, and the spatial arrangement of trees. Then parallel-ray geometry is used to describe the illumination of the three-dimensional cone and the shadow it casts. This approach has further been developed and improved upon, by compositing several crown fractions or applying non-quadratic shapes for a more realistic representation, more accurately describing the canopy by accounting for crown asymmetry and variations in foliage density. However, these more realistic three-dimensional representations require a larger set of input data and parameters, some of which can only be measured in the field with difficulty (Ligot et al., 2014). Examples of shapes used in these forest representations are shown in Table 1.

**Table 1:** Examples of 3D geometric crown models used in RTMs. Adapted from Ligot et al. (2014).

	Quadratic shapes	Combination of quadric shapes	Combination of degenerated shapes
Example shapes			
<hr/>			
# of parameters	3	2-4	8-18
References	Li and Strahler (1985); Paquette et al. (2008); Stadt and Lieffers (2000)	Gersonde et al. (2004)	Da Silva et al. (2012); Cescatti (1997)

As mentioned before, canopy structure is an important factor in the variability of radiation within forests and drives photosynthesis within the canopy, light-use efficiency and ecosystem gas exchange (De Pauw et al., 2022; Sage and Kubien, 2007; Kull and Kruijt, 1998; Kükenbrink et al., 2021). The simplification of vegetation structure has shown to be the cause of an underestimation of photosynthesis and a misrepresentation of forest gas exchange (Braghieri et al., 2020; Damm et al., 2020). Hence, for RTMs to accurately simulate light conditions within forests, a detailed description of the vertical and horizontal arrangement of vegetation is necessary. The advent of new laser-scanning technologies, especially the affordable and practical terrestrial laser scanning (TLS), provides new possibilities to quantify forest ecosystem structure at a high resolution (Danson et al., 2018). Various approaches have been developed over the last decade to parameterize RTMs using a TLS-based acquisition of canopy structure.

Van der Zande et al. (2010, 2011) proposed a "Voxel-Based Light Interception Model" (VLIM), in which based on TLS data a voxel-based 3D representation of the forest stand is constructed to model light interception. VLIM estimates the percentage of above-canopy light at any point within the canopy. This method involves separating the stem from the foliage voxels and estimating the LAI of the foliage voxels using the calculated contact frequency of every laser beam penetrating the voxel. VLIM then simulates virtual rays of light in the 3D scene and calculates the absorption, scattering and transmission of each of the vegetation voxels. However, this approach was only applied on a completely virtual forest or didn't compare results to validation data from in-situ measurements.

A similar but more complex voxel-based approach was developed by Cifuentes et al.

(2017). To classify TLS point clouds into leaves or trunks (including larger branches), researchers utilized an octree-based algorithm that recursively subdivides the 3D space into smaller cubes (octants) to identify connected structures. Trunks were then identified based on specific minimum height, width, and length requirements, while the remaining points were classified as leaves. Using the physically based raytracer (PBRT) (Pharr et al., 2016), hemispherical images were rendered to calculate the simulated PAR values which were compared to PAR values from a spectroradiometer and actual hemispherical photographs at the same location. This approach showed relatively poor correlations, which were likely caused by occlusion effects due to dense forest canopies and the limited range of the LiDAR scanner or faulty classifications of stems and foliage.

To address the issue of spatial uncertainty introduced by voxelizing point cloud data, Calders et al. (2018) proposed a novel method to generate a virtual forest from highly detailed leaf-off TLS data. During the tree segmentation process, stems are identified by segmenting a height slice of the point cloud (1-3 meters above ground), whereas the crown points are isolated by identifying point clusters based on point density in height slices along the tree. The individual tree point clouds are then used to generate quantitative structure models (QSMs) (Raumonen et al., 2013). The QSMs are created by fitting trunk or branch cylinders at specific trunk lengths, and their diameters are estimated using least squares circle fitting on the point cloud slices. Then, leaves are added using the Foliage and Needles Naïve Insertion (FaNNI) algorithm, where leaf shapes and a size distribution are defined and leaves are added to the QSM based on a defined leaf area density distribution, which determines the probability of leaves on different parts of the tree. Spectral characteristics of leaves, bark, and understorey were based on spectrometer measurements in the field. In-situ digital hemispherical photographs and Sentinel-2 satellite images were then rendered using the librat Monte Carlo Ray Tracing (MCRT) model (Lewis, 1999). Although these images achieved a strong agreement with real-world data, this approach still presents several technical and practical challenges. High-quality and high-density leaf-off TLS data are crucial for the process of creating realistic QSMs. This creates the need for a large amount of scanning angles and introduces a long time difference between the scan and the gathering of validation data during leaf-on conditions, making comparisons challenging due to possible changes in the ecosystem. Further, QSMs have several known issues and challenges, as they often overestimate the radii of thin branches and frequently require manual adjustment of parameters which can lead to a labor-intensive process (Hackenberg et al., 2015; Morhart et al., 2024).

Kükenbrink et al. (2019) used leaf-on TLS data to parametrize the Discrete Anisotropic Radiative Transfer (DART) model (Gastellu-Etchegorry et al., 2015) to accurately simulate the irradiance field around an isolated tree. To extract the tree trunk and major branches, a reflectance threshold was set. LiDAR returns have varying intensity values when they hit foliage compared to wood. By analyzing the distribution of these intensity values, specific thresholds can be set to differentiate between the two types of points. Although there are more sophisticated stem and foliage separation methods, the simplicity and computational efficiency of a thresholding approach makes it practical for large-scale studies and consistent application across various datasets. Thresholding avoids the complexity and extensive calibration more complex methods require (Vicari et al., 2019; Xu et al., 2021), which can be challenging in variable field conditions.

From the extracted trunk and branch point cloud a 3D mesh was created using screened Poisson reconstruction method in MeshLab (Cignoni et al., 2008). To represent the foliage researchers utilized the AMAPvox R package (Vincent et al., 2017) developed by "botAnique Modélisation de l'Architecture des Plantes et des végétations", to process the separated foliage point cloud data and generate a voxel file with Plant Area Density (PAD) ( $\text{m}^2/\text{m}^{-3}$ ) estimation per voxel. As the emitted laser pulse from the scanner hits material along its path the sensor registers the backscattered energy from each target. The amount of returned energy is dependent on the distance from the target and also on the optical properties of the target. Based on this the AMAPvox software computes an estimated transmittance of vegetation as the ratio of the sum of energy exiting a voxel to the sum of energy entering the same voxel. A spatially hierarchical model is subsequently applied to calculate estimates of every voxel's transmittance. Plant area density (PAD) profiles are then computed from the local transmittance values by applying Beer Lambert's turbid medium approximation (Vincent et al., 2017). AMAPvox outputs a voxel space array file, with voxel Y, Y and Z positions and various parameters per voxel (e.g. number of hits, number of pulses, cumulated path length, etc.) from which the PAD can then be calculated.

Utilising the "Radiative Budget", a DART tool that calculates 3D irradiance profiles, the researchers validated the simulation outputs with irradiance measurements from the field spectroradiometers. In the 2021 study, this approach was then applied to two contrasting forests for which the extinction of PAR by the canopy was simulated based on a combination TLS and unmanned aerial vehicle (UAV) laser scanning data (Kükenbrink et al., 2021). In both studies, the DART simulation outputs showed a

strong agreement between modeled and measured values. To showcase the implications of accurately quantifying surface irradiance, the researchers analyzed the effect of utilizing TLS-parameterized DART scenes to model top-of-canopy (ToC) reflectance and subsequently derive the chlorophyll index and carotenoid index, comparing the results to those obtained using apparent ToC reflectance under the assumption of homogeneous illumination. They found overestimations of the vegetation indices of up to 14%, highlighting the impact of detailed RTM parameterization on the accuracy of vegetation indices.

Liu et al. (2022) investigated the effects of different 3D forest stand reconstruction methods on the accuracy and efficiency of RTMs. While comparing the aforementioned approach by Calders et al. (2018) with a voxel-based method at varying voxel sizes, the researchers found that the voxel-based simulations showed significant deviations in directional reflectance and spectral albedo compared to 3D-explicit models, particularly when using larger voxel sizes. Further, the benefit of voxel-based methods regarding computational efficiency was only prevalent for voxel sizes starting at 1 meter. Smaller voxel sizes required significantly more computational resources, proving to be impractical for large-scale applications. Leading the researchers to recommend an approach using explicit 3D reconstructions for applications demanding a high accuracy, whereas a 1m voxel-based approach is recommended for large-scale implementations as it offers a compromise between computational efficiency and accuracy.

The Radiative Transfer Model Intercomparison (RAMI) (Widlowski et al., 2015) is a framework designed to evaluate and compare the performance of various RTMs used for simulating light interaction with vegetation canopies. It uses standardized scenarios and datasets to assess the accuracy, efficiency, and consistency of various RTMs. Among these RTMs, including for example LESS (Qi et al., 2019), FLIGHT (North, 1996), RAYTRAN (Govaerts and Verstraete, 1998), and PBRT (Pharr et al., 2016), the Discrete Anisotropic Radiative Transfer (DART) model (Gastellu-Etchegorry et al., 2015) stands out as a particularly robust and versatile platform (for a more comprehensive overview of the benchmarked RTMs, see Widlowski et al. (2015)). DART can accurately represent complex three-dimensional forest structures and handle both voxel-based and explicit object-based models. Since its development in 1992, DART has evolved into one of the most comprehensive RTMs available. It simulates the three-dimensional radiation balance (intercepted, absorbed, scattered, and emitted radiation) and remote sensing observations of natural (e.g. forests and agriculture) and urban landscapes, accounting for topography and atmosphere across

the entire optical domain. DART is adaptable to a variety of experimental conditions (e.g., atmospheric conditions, date and sun direction) and instrumental configurations (e.g., viewing direction, altitude, spatial or spectral resolutions) (Figure 1). Three operating modes exist within DART: flux tracking (FT), Forward Monte Carlo + Ray tracking (RC), and Lux. DART-Lux was implemented in 2018 and compared to the other two modes of functioning, presents a step forward in accuracy and efficiency. Adapted from the physically based and unbiased rendering engine LuxCoreRender (LuxCoreRender Team, 2024), its computation time and RAM-need can be over 100 times lower than DART-FT, this is also due to only tracking radiation that impacts the signal forming the sensor observation. In DART-Lux the scene is not represented as a voxel array as in the other two modes. Here volumes can take any shape. Vegetation such as grass or tree crowns are often simulated as voxel plots in DART. Voxel plots can be defined as a turbid medium with an infinite number of infinitely small flat triangles characterized by density, angular distribution, and

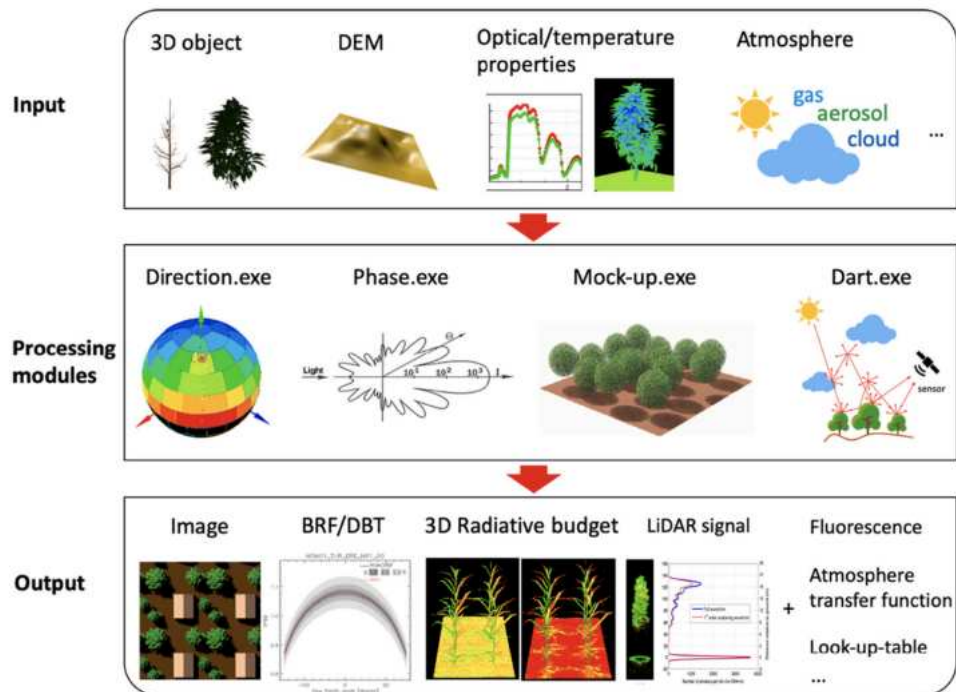


**Figure 1:** Illustration of the DART framework and its four modules (Direction, Phase, Mock-up, Dart) to simulate remote sensing and radiative budget products for many instrumental or experimental configurations (Gastellu-Etchegorry et al., 2015)

optical properties.

DART also allows for the import of detailed 3D models composed of triangles, with the possibility of defining optical properties for each 3D object or individual groups of polygons within this object. During ray tracing, two types of radiation interactions are modeled: volume interactions within turbid voxels and surface interactions on the triangles. Triangles can have any orientation, area and optical property (Lambertian or specular reflectance, isotropic or direct transmittance). To simulate the atmosphere, DART has the option to use standard gas and aerosol models as contained in MODTRAN (MODerate resolution atmospheric TRANsmission) (Berk et al., 1989). MODTRAN is a software tool used for modeling atmospheric propagation of electromagnetic radiation, primarily for remote sensing and atmospheric research applications. Further details of the DART model and examples of DART simulations can be found in (Gastellu-Etchegorry et al., 2015) and more detail on DART-Lux in (Wang et al., 2022).

## 1.2 Research Objective

Despite the significant advancements over the last decades in both in-situ measurement techniques and RTM approaches, accurately quantifying light distribution within complex forest structures remains challenging. Current methodologies, using voxel-based models or complex tree reconstruction processes, often face limitations such as occlusion effects, spatial uncertainties, labor-intensive processing and computational inefficiencies. Few studies have extensively validated their reconstruction approaches with comprehensive in-situ measurements.

In this thesis, I implement a novel voxel-based surface reconstruction approach developed by Julian Frey and Zoe Schindler (Frey et al., 2024) to directly derive explicit wood and leaf geometries from TLS data. I present a proof-of-concept workflow for parameterizing a DART scene of a single apple tree based on these geometries and simulating PAR sensors at specified positions underneath the tree. The simulation results are validated against in-situ PAR measurements and compared to a voxelized foliage approach similar to the method utilized by Kükenbrink et al. (2021, 2019) to quantify differences in accuracy and computational efficiency. The implemented approach is expected to have highly accurate PAR values and show a significant improvement compared to the voxel-based approaches.

## 2 Materials and Methods

An overview of the methodology and workflow applied in this thesis is given in Figure 3. Table 2 lists the main software utilized. All scripts and example data are available on GitHub at the following link: [github.com/PatrickMcClatchy/dart-par](https://github.com/PatrickMcClatchy/dart-par)

### 2.1 Study Site

The study site is located within a peri-urban environment in Dietenbach Park, Freiburg, southwest Germany, on a flat meadow at approximately 230 m a.s.l. (Figure 2, 48°00'03.1"N, 7°48'01.0"E). The methodology was applied to a single apple tree (*Malus domestica* Borkh.). The area around the tree is free of large buildings or dense vegetation that could cast shadows or cause reflectance. Measurements were taken in August 2023 under warm, sunny conditions with a mean global radiation of 240 J/cm<sup>2</sup>/h and an average temperature of 28°C. The sky was clear, with no visible clouds.

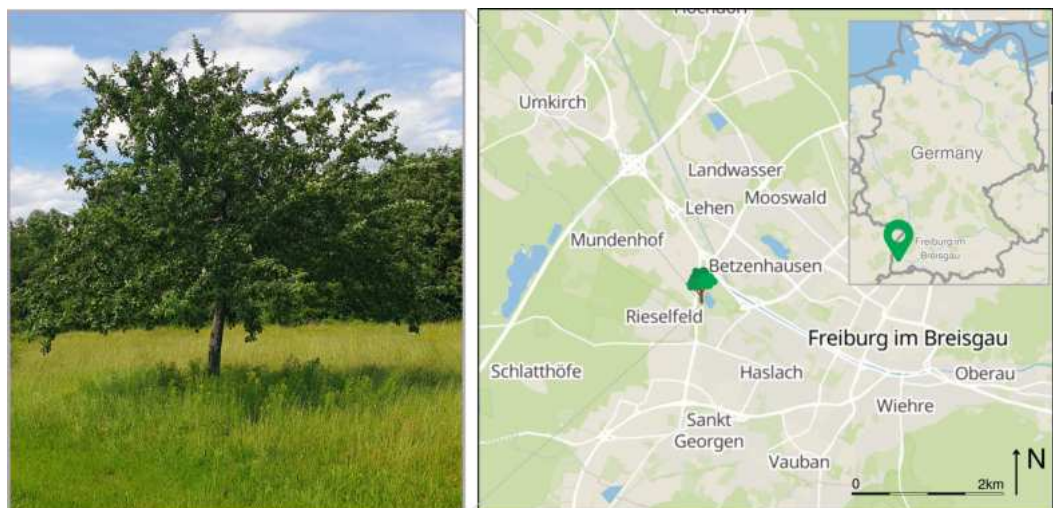


**Figure 2:** Location of the study site and image of the target tree (*Malus domestica* Borkh.); Freiburg im Breisgau, 48°00'03.1"N, 7°48'01.0"E; Map data from OpenStreetMap (2017).

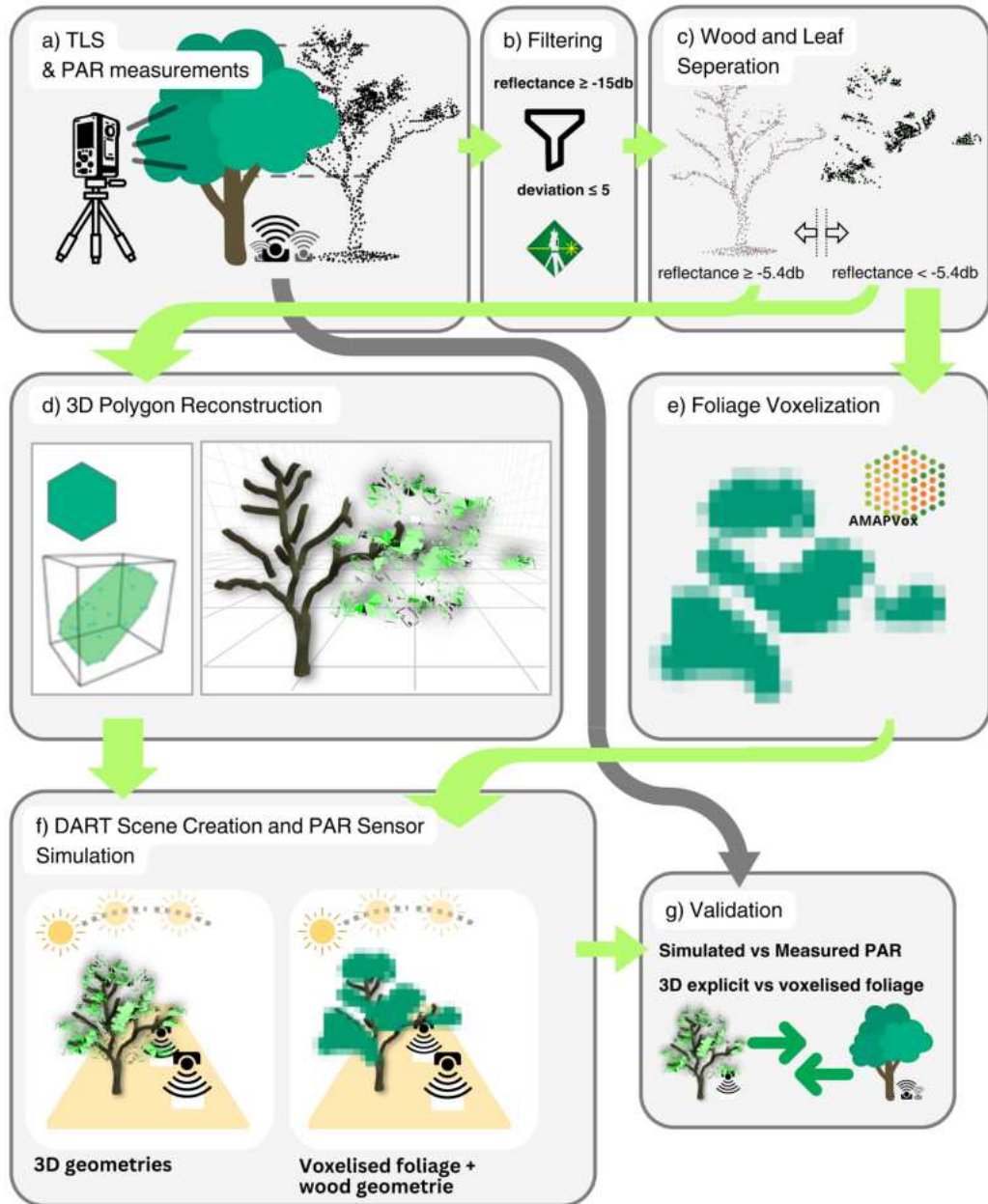


**Figure 3:** Exemplary overview of the workflow applied in this thesis to simulate PAR values within a DART scene based on TLS data.

a) TLS and PAR measurements of the study area b) Filtering c) Wood and leaf points separation by reflectance threshold d) 3D polygon reconstruction of wood and leaf geometries e) Voxelization and PAR estimation of foliage points f) Dart scene parameterization and PAR sensor simulation (Radiance cameras facing toward a white lambertian surface) g) Validation of simulated PAR values with in-situ measurements and comparison between scenes

**Table 2:** Software used for tree reconstruction and consequent radiative transfer modelling

Processing Step	Reference	Link
Tree Delineation	CloudCompare (version 2.11.3) (2023)	<a href="https://www.danielgm.net/cc/">https://www.danielgm.net/cc/</a>
Voxelization	Vincent et al. (2017)	<a href="https://github.com/umr-amap/AMAPVox">github.com/umr-amap/AMAPVox</a>
Geometry Construction	Frey et al. (2024)	<a href="https://github.com/JulFrey/dotshadow">github.com/JulFrey/dotshadow</a>
Scene Parameterization	de Boissieu et al. (2019)	<a href="https://pytools4dart.gitlab.io/pytools4dart">pytools4dart.gitlab.io/pytools4dart</a>
Radiative Transfer Modelling	Gastellu-Etchegorry et al. (2015)	<a href="https://dart.omp.eu">dart.omp.eu</a>

## 2.2 PAR Measurements

To measure PAR, 60 sensors (SQ-110, Apogee Instruments, Logan, Utah, USA) were placed around the north side of the tree (Figure 3a). The sensors were grouped in sets of 12 and connected to data loggers (Adafruit Feather 32u4 Adalogger, Adafruit Industries, New York City, New York, USA) and mounted to wooden frames (2 m  $\times$  3 m) to increase their visibility within the TLS data, to elevate them above the grass, and to level them. The experimental design is illustrated in Figure 4. Each sensor recorded PAR at 1-minute intervals from 12:10 to 17:15 CEST. To capture shade dynamics in the afternoon, one of the structures was moved from a purely sunny position northwest of the tree to the east side. The measurements taken during this movement were excluded from the data to ensure accuracy. The geographic positions of the sensors were manually recorded within the TLS data to ensure the most accurate match between TLS and sensor data. Additionally, data on global and diffuse radiation was obtained at 5-minute intervals from a German Weather Service station located 3 km from the research site.

## 2.3 LIDAR Data

The target tree was scanned from eight different positions, each approximately 10 m away from the stem, using a RIEGL VZ-400i laser scanner (RIEGL Laser Measurement Systems GmbH, Horn, Austria) (Figure 3a). The scanner had an angular resolution of 0.04° and a pulse rate of 1,200 kHz. Scan positions were recorded using an integrated GNSS system, which received live corrections from a nearby base station. The scans were automatically co-registered on the device using the GNSS data and onboard measurements from an inertial measurement system. The co-registration was later inspected visually. To improve data quality, noise points were filtered out, removing points with very low reflectance ( $\leq$  -15 dB) and high pulse deviation ( $\geq$  15) (Figure 3b). The filtered point clouds were then combined using a 1 cm voxel

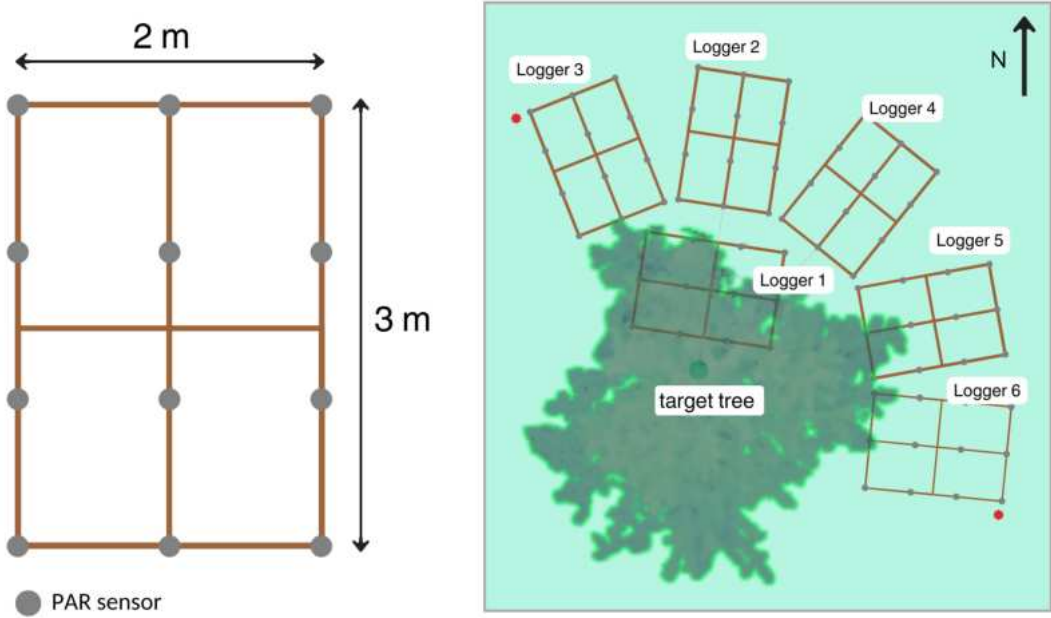


**Figure 4:** Experimental setup of quantum PAR sensors (SQ-110, Apogee Instruments) around the target tree. The red stars indicate the structures which were moved during the course of the day. Adapted from (Schindler et al., 2024).

grid. For each voxel, the center of gravity was calculated to exclude duplicated points and homogenize the point density. All pre-processing was conducted using RiSCAN software (v 2.18.1, RIEGL Laser Measurement Systems GmbH, Horn, Austria). The target tree was manually separated within the point cloud and all points of the tree were classified into leaf and wood points based on a reflectance threshold of -5.4 dB (Kükenbrink et al., 2021) (Figure 3c).

## 2.4 Stem and Foliage Model Construction

All following processing of the TLS data was done in the R statistical software (v4.2) within the R Studio IDE (R Core Team, 2022). The stem and foliage reconstruction approach developed by Julian Frey and Zoe Schindler (Frey et al., 2024) was applied to the target tree point cloud to obtain 3D geometries (Figure 3d).

Figure 5 illustrates this workflow to assign geometries to the voxels' points in detail. In this process, all points are assigned to a voxel grid of 5 cm edge length. For each voxel, a class of either leaf or wood is assigned based on the class of the majority of the contained point classes within the voxel. If a voxel contains at least three points,

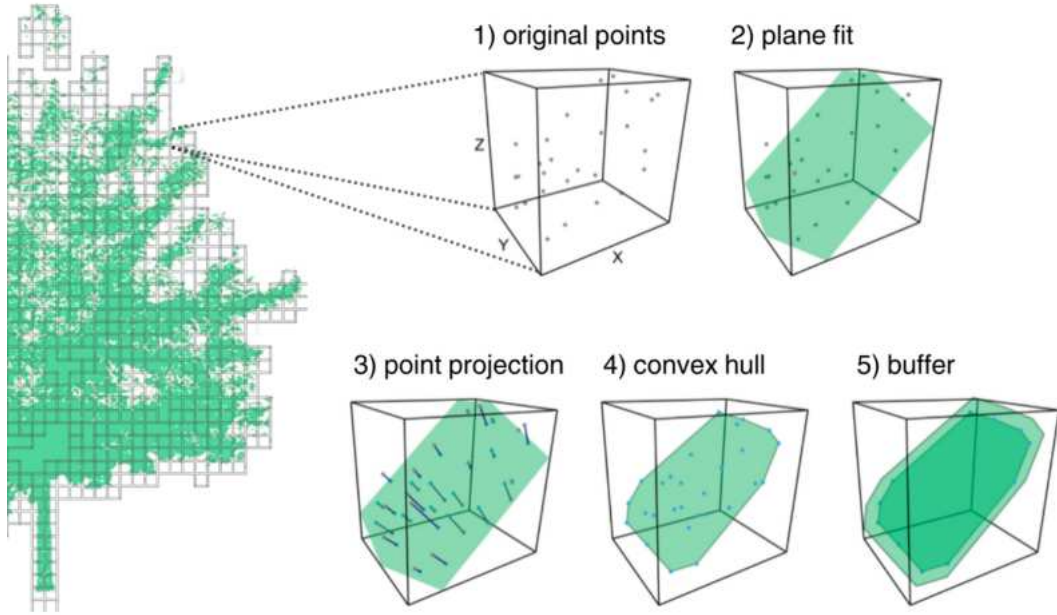


**Figure 5:** Illustration of the process to assign geometries to the points within each voxel to construct explicit 3D models of foliage and wood. Adapted from Frey et al. (2024).

a best-fitting plane is determined using Singular Value Decomposition. The points are then projected onto this plane, and a convex hull is computed to form a polygon that represents the shape of the points within that voxel. To avoid artificial gaps between adjacent polygons, a buffer is applied to the convex hull. This buffer is half of the theoretical distance between points based on the point cloud downsampling resolution. In cases where a voxel contains fewer than three points, a six-sided polygon with a diameter of a third voxel size with the center at the points' location and a random rotation was generated. This approach aims to resemble the original leaf area, distribution and angles as closely as possible. The convex hulls and six-sided polygons were then triangulated to form mesh polygons using the `rgl` package (Murdoch and Adler, 2022). This process involves generating vertex and face definitions for each polygon and writing the results to wavefront OBJ files. DART considers the object to be in an x-forward, y-up system. Hence, the vertex coordinates must be written in the order of `v y z x` inside the `.obj` file.

## 2.5 Voxelization

Using the `AMAPvox` R package (v2.0.2) (Vincent et al., 2017) the point cloud of the target tree was voxelized (Figure 3e). `AMAPvox` allows for the direct import of a RiScan project folder, from which the scanner positions of each scan are then read. Voxels with a majority of laser returns classified as wood were excluded from further processing, as major tree trunks and branches violate the turbid medium assumption for the selected voxel sizes. Isolated voxels, with only empty voxels in their Moore neighborhood, as well as voxels with less than 50 echos, were removed (Vincent et al., 2017).

For the consequent calculation of PAD the leaf angle distribution was assumed to be planophil, as suggested for the *Malus* genus by Pisek et al. (2013). Single leaf area was set to 10 cm and the maximum PAD value was to 5 m<sup>2</sup>/m<sup>3</sup> (Vincent et al., 2017).

## 2.6 DART Parametrisation

The radiative transfer model used in this study was the DART v5.10.2 (Gastellu-Etchegorry et al., 2015). The DART-Lux mode was used with the sun and atmosphere as the only radiation sources. For the parameterization and execution of the DART simulations, the Python API `pytools4dart`, developed by de Boissieu et al. (2019), was used. This API handled the creation of multiple scenes, running sequences, and processing of the output data, making the process more reproducible and less labor-intensive compared to using the DART graphical interface. The `pytools4dart` module was used in Python 3.8, and the scripts were written in Jupyter Notebook (Kluyver et al., 2016) to provide explanations and ensure the parameterization was reproducible. Three separate DART scenes were created with:

- a. Explicit 3D geometries for both wood and foliage
- b. Explicit 3D geometries representing wood and voxelized foliage at a voxel size of 0.2 m
- c. Explicit 3D geometries representing wood and voxelized foliage at a voxel size of 1 m

## Coordinate Transformation and Import

To import the assets into the DART scene a transformation of coordinates is necessary. A DART scene has a Cartesian coordinate system in which coordinate values are only positive, with a coordinate origin (0,0) in the top left corner and an axis order of  $y, x, z$ , resulting in an inverted vertical x-axis (Figure 6). As the point cloud coordinates are based in the format of RiScan project coordinates, a transposition of the x-, and y-axis and a following inversion of the x-axis is necessary. PAR-sensor positions were transformed from UTM to project coordinates and then translated to the DART scene coordinate system.

To achieve only positive coordinate values, a global coordinate offset is calculated based on the difference between the geographical center of the imported wavefront OBJ and scene center (10,10), placing the center of tree geometries in the center of the scene.

For the import of AMAPvox files, pytools4dart provides the `voxreader` module, which helps to manage voxelized PAD data and prepares them to define turbid plots in the DART simulation. The voxel file coordinates were transformed and the global offset was added by rewriting the extent of the voxel file in its header.

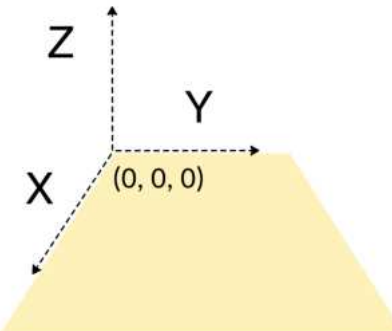


**Figure 6:** DART scene coordinate system.

## Atmosphere and Radiative Sources

In the DART scenes simulated in this thesis, the midlatitude summer gas model and the rural aerosol model with a visibility of 23 km were used, resembling the weather conditions of the day of PAR measurements the closest. Both models are contained in MODTRAN (Berk et al., 1989).

A single band of input radiation (400-700 nm) was defined for the simulation, with the sun as the only radiation source. The bottom of atmosphere (BOA) irradiance was calculated using the DART Analytical Model. The sun azimuth and height were determined by specifying the geographical position, time zone, and exact date and time. For each of the scenes, simulations were run in 10-minute timesteps from 12:00 to 18:00 for the date of August 10th, 2023, resulting in 36 runs for each scene. This was achieved by writing a sequencing loop with an adjusted sun angle for each simulation iteration. Although DART includes a `sequence`-module, this tool caused issues when combined with the method used to define the simulated sensors.

### Optical properties

An optical property has to be assigned to each surface or object within the scene. DART includes databases for the spectral properties of various elements. Figure 7 illustrates the spectral response within the PAR range of all optical properties of the objects or surfaces within the simulated DART scenes. For the leaf optical properties (LOP) the spectral database `leaf deciduous` was defined. For the ground `citrus orchard ground` and the trunk `bark deciduous`.

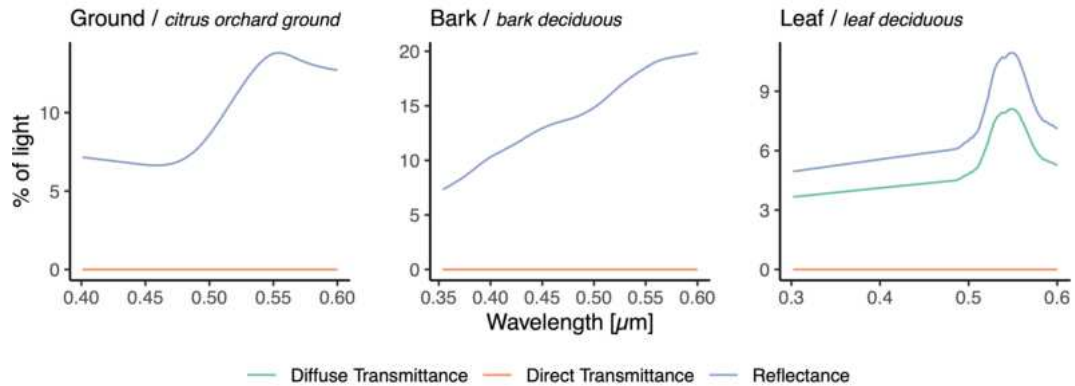


**Figure 7:** Figure of the spectral responses of the optical properties defined in the DART scenes, showing the percentage of light either which is either diffusely transmitted, directly transmitted or reflected by the respective surfaces or media.

## PAR Sensor Definition

To represent the in-situ PAR measurements at the study site, the sensor type Perspective Camera/Pinhole was used. This simulated camera sensor captures radiance with a defined focal length, sensor size and viewing direction. As no DART function exists to define multiple sensors, a single sensor was created within the graphical interface. Based on the resulting XML node, a user-defined function was written to allow the definition of various sensor positions and configurations.

To simulate the at-sensor PAR irradiance, a flat rectangle target object was created in Blender and placed at the positions of the actual PAR sensors. A Lambertian optical property was created with 100% reflectance across the entire spectrum and assigned to the targets. Figure 8 illustrates the simulated sensor definition within the scene. The radiance camera was specified with a single pixel  $5 \times 5$  cm sensor and a focal length of 10 cm, positioned 10 cm above and pointed downwards at the target. This results in the radiance values of an area of  $0.2 \text{ cm}^2$  being averaged. As the defined optical properties of the target reflect light uniformly in all directions and across all wavelengths, these radiance values can be integrated over the hemisphere above the surface to derive the irradiance.

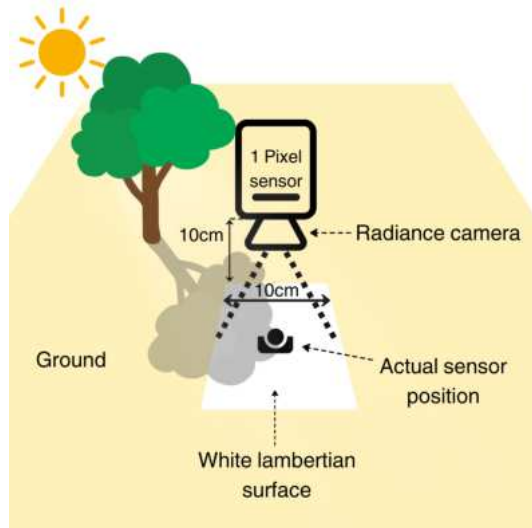


**Figure 8:** Illustration of simulated PAR sensor setup within the DART scene. The radiance camera captures radiance of all surfaces within the frame. It is directed at a white lambertian surface which reflects uniformly bright from all directions of view and reflects the entire incident light. This allows for the calculation of surface irradiance at the actual sensor position.

The at-surface irradiance is therefore calculated by:

$$E = \pi L \quad (1)$$

with  $E$  being the irradiance and  $L$  the radiance. To convert the simulated PAR surface irradiance ( $\text{W m}^{-2}$ ) to PPFD ( $\text{mol m}^{-2}$ ), the following formula was used:

$$\text{Photon Flux } (\mu\text{mol m}^{-2}\text{s}^{-1}) = \left( \frac{\text{Irradiance } E \left( \text{W m}^{-2} \right)}{\frac{h \cdot c}{\lambda_{\text{avg}}}} \right) \times \left( \frac{1}{N_A} \right) \times 10^6 \quad (2)$$

where  $h$  is Planck's constant ( $6.626 \times 10^{-34} \text{ J}\cdot\text{s}$ ),  $c$  is the speed of light ( $3 \times 10^8 \text{ m/s}$ ),  $\lambda_{\text{avg}}$  is the average wavelength of the PAR range (550 nm), and  $N_A$  is Avogadro's number ( $6.022 \times 10^{23} \text{ photons/mol}$ ). With this conversion in-situ measurements and simulated values can directly be compared (dos Reis and Ribeiro, 2020; Yamashita and Yoshimura, 2019).

## 2.7 Validation

To validate the simulated PAR values, the temporal dynamics of the PAR values were examined by plotting the time series of both simulated and measured PAR values for all sensor locations. This was done to evaluate if the simulations accurately captured the variations in PAR due to changes in solar angle and tree shading. Additionally, to assess the accuracy of the simulated PAR values, Pearson's correlation coefficient  $r$  was calculated for the measured PAR and the simulated PAR values at the scene, logger and sensor level, for all three scenes respectively. Further, to compare the simulated and measured values without the effect of daily radiation patterns, PAR measurements were classified. At each time step  $i$ , values of  $\text{PAR}_i$  greater than or equal to  $\text{max}(\text{PAR}_i) - 190 \mu\text{mol m}^{-2} \text{s}^{-1}$  were classified as light, those less than or equal to  $\text{min}(\text{PAR}_i) + 75 \mu\text{mol m}^{-2} \text{s}^{-1}$  were classified as shade and intermediate values were classified as semi-shade (Schindler et al., 2024). From this categorization, confusion matrices were constructed to evaluate the accuracy of the simulations in predicting each of the three light levels.

### 3 Results

#### 3.1 TLS

After co-registration, filtering and tree delineation the final point cloud of the target tree consisted of 1,29 million points. Wood and leaf separation, by ways of the reflectance threshold, resulted in 121,774 points classified as wood and 1,167,327 points classified as leaves (Figure 9a). Although the point cloud of the target tree did not present the expected clear bimodal distribution of reflectance (Figure 9b), visual inspection confirmed the thresholding approach effectively separated wood and foliage.

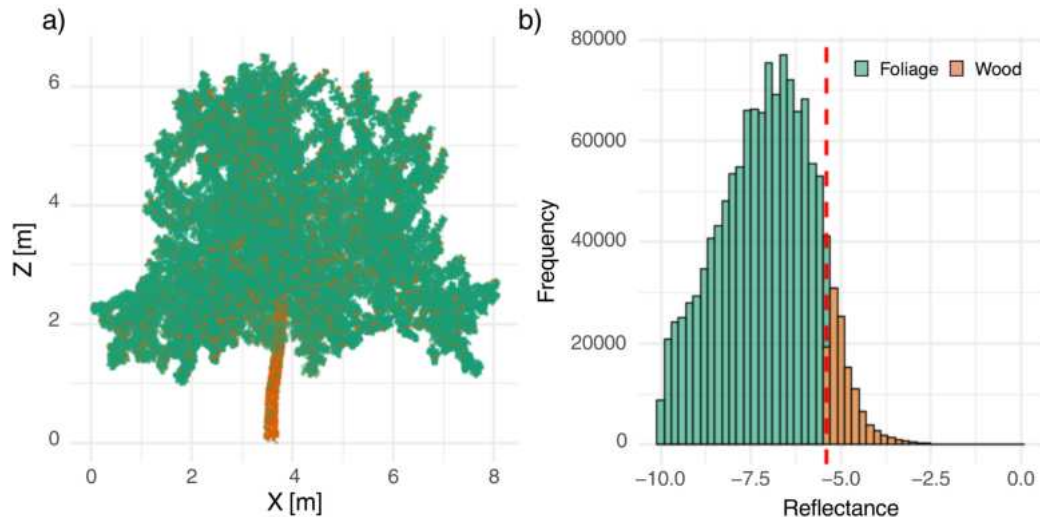


**Figure 9:** a) Delineated and filtered target tree point cloud classified into wood (brown) and foliage (green) b) Distribution of reflectance of the point cloud returns. The dotted red line indicates the threshold value for separation at -5.4 dB.

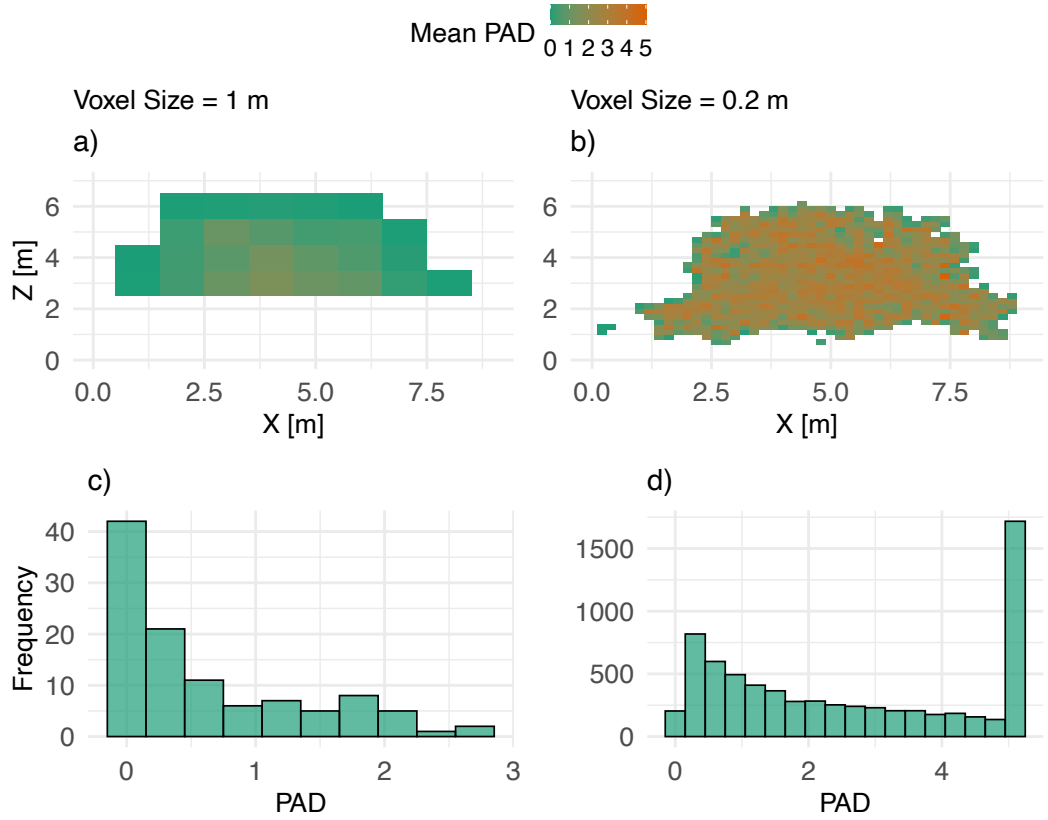


**Figure 10:** Distribution of PAD in the voxelized foliage point cloud derived from AMAPvox. a) Average PAD for  $(X, Z)$  (voxel size of 1 m); b) Average PAD for  $(X, Z)$  (voxel size of 0.2 m); d) Histogram of PAD values (voxel size of 1 m); c) Histogram of PAD values (voxel size of 0.2 m)

### 3.2 Voxelization and PAD

The voxelization, consequent removal of the majority of wood voxels and calculation of PAD, resulted in 6960 voxels for the voxel size of 0.2 m with a mean PAD of  $2.5 \text{ m}^2/\text{m}^3$  and a maximum PAD of  $5.0 \text{ m}^2/\text{m}^3$ . For the 1 m voxel size, the resulting voxel array consisted of 108 voxels with a mean PAD of  $1 \text{ m}^2/\text{m}^3$  and a maximum PAD of  $3.0 \text{ m}^2/\text{m}^3$ . For the voxel size of 0.2 m, a clear peak at a PAD of  $5 \text{ m}^2/\text{m}^3$  (the set max. PAD) is visible. Figure 10 illustrates the spatial and frequency distribution of PAD for both voxel sizes. The distribution shows higher PAD values in the inner crown, where leaf density is greatest, and lower values towards the edges of the canopy. This pattern is consistent across both voxel sizes. Figure 11b) and Figure 11c) provide 3D representations of both foliage voxel arrays imported into the DART scenes.

### 3.3 Stem and Foliage Model Construction

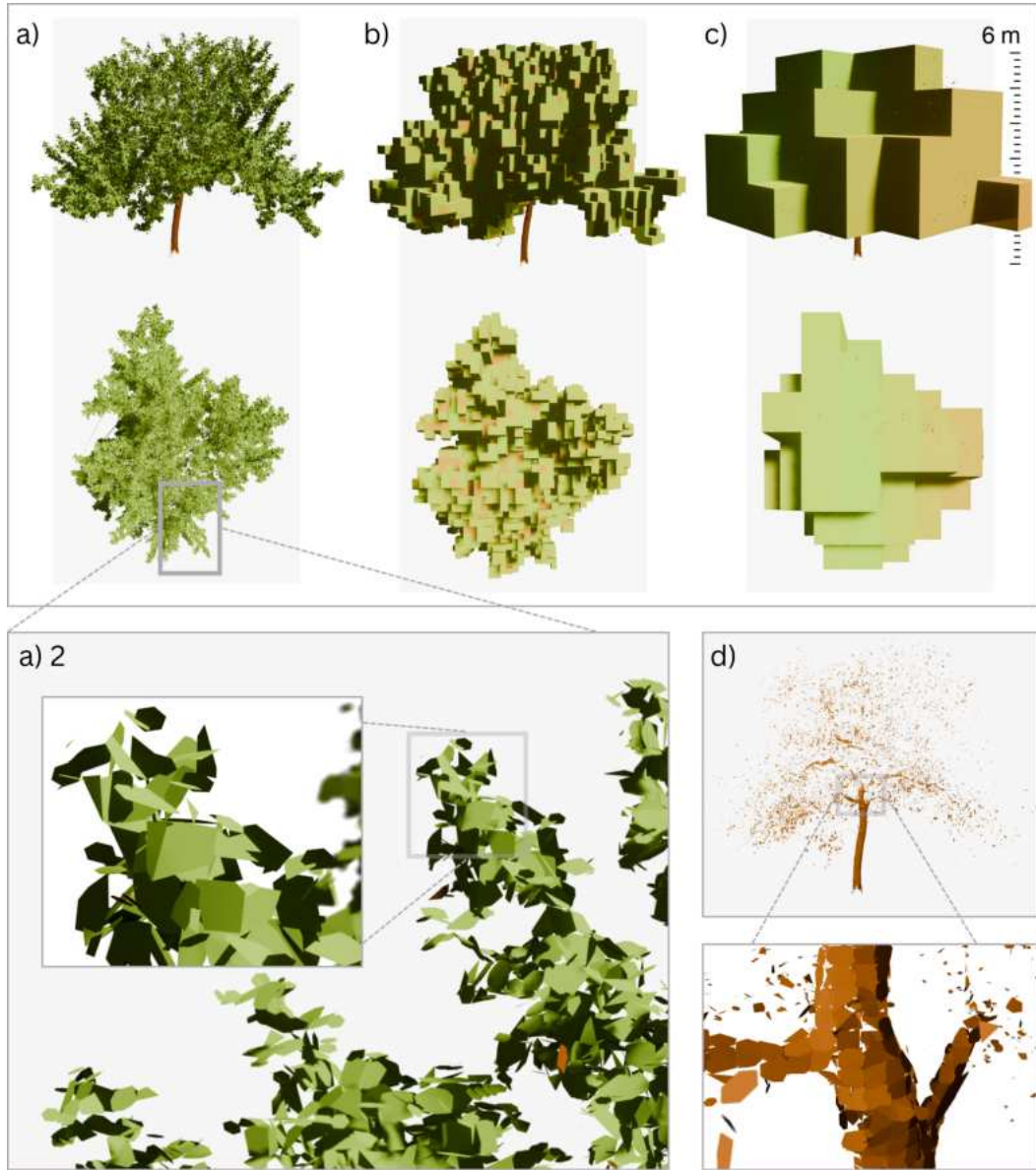


**Figure 11:** 3D renders of the three representations of the target tree utilised in each respective scene. Front and nadir view of : a) Explicit geometries for both wood and leaves; b) Voxelized leaves with PAD. Voxel size of 0.2 m; c) Voxelized leaves with PAD. Voxel size of 1 m; d) close-up of explicit leaf geometries; e) Reconstructed stem and branch geometries, used in all three scenes; Trees rendered using the open-source 3D software Blender (Blender Development Team, 2024).

During the construction of the explicit 3D geometries of wood and foliage, 147,098 of the 5cm voxels were classified as foliage and 9511 as wood. For each of these voxels either a single polygon or, in cases where a voxel only contained two points, two polygons were written. 40,190 foliage voxels, more than a third of all foliage voxels, contained only one or two points, resulting in six-sided polygons. 5236 wood voxels only contained one or two points, resulting in more than half of the classified wood voxels being represented as six-sided polygons. Overall this resulted in a Wavefront OBJ mesh with 185,732 faces. Figure 11a) shows the 3D representations of both the foliage and wood geometries combined, whereas Figure 11d) depicts only the wood geometries. This shows the rather fragmented reconstructed surface of the stem and branches. Visually, the reconstructed geometries of the foliage seemed to agree well with the TLS point cloud. Showing a similar extent and overall shape, although possibly differing leaf angles (Figure 11a).

Figure 12 shows a screenshot of the DART 3D scene viewer, illustrating the explicit geometry scene with foliage and wood polygons, as well as white Lambertian surfaces used as targets for the simulated PAR measurements.

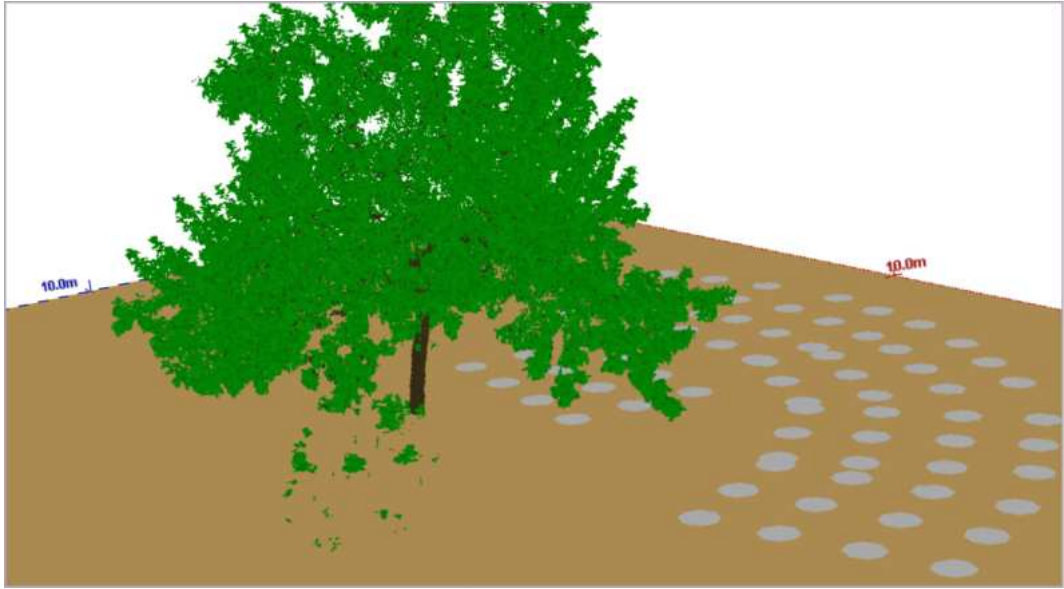


**Figure 12:** Screenshot of the DART 3D viewer showing the scene with the explicit geometry tree model and white Lambertian surfaces as used PAR sensor targets (grey circles).

## 3.4 Simulated PAR vs. Measured PAR

### 3.4.1 PAR measurements

A total of 17,496 PAR measurements were logged at 1-minute intervals from 12:10 to 17:10. The radiation recorded by all sensors during the sample period is displayed in Figure 13a. The measured PAR values varied strongly across different sensor positions, reflecting the shading patterns surrounding the tree caused by the canopy. With some loggers exhibiting overall lower values over the measurement period than others (e.g. Logger 1) due to their position directly underneath the canopy.

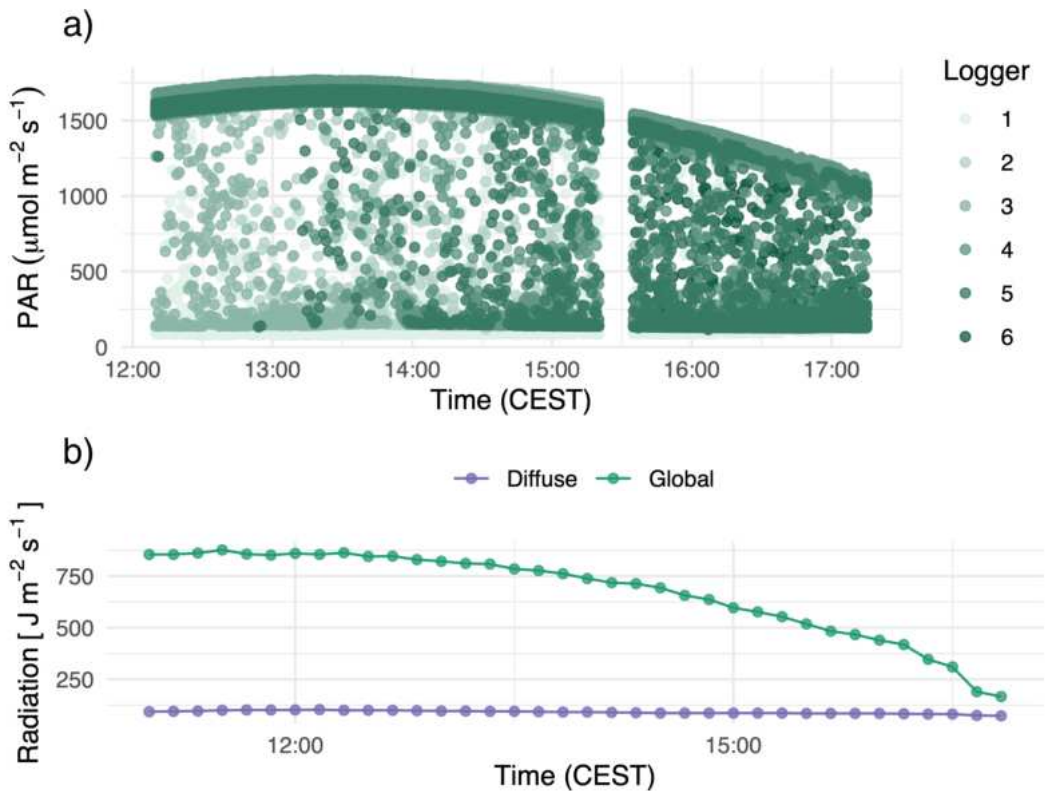


**Figure 13:** Radiation during the measurement period. a) In-situ quantum sensor measurements by logger. b) Reference radiation data from the Deutscher Wetterdienst (2024) (diffuse, global).

The average PAR values of the loggers ranged from  $453 \mu\text{mol m}^{-2} \text{s}^{-1}$  to  $1460 \mu\text{mol m}^{-2} \text{s}^{-1}$ . The minimum PAR values recorded were between  $79.2$  and  $140 \mu\text{mol m}^{-2} \text{s}^{-1}$ , and the maximum PAR values ranged from  $1532$  to  $1768 \mu\text{mol m}^{-2} \text{s}^{-1}$ . For

each sensor separately, measured PAR values often showed a high temporal variability, depicting the small-scale changes in light availability underneath the canopy, likely caused by the shadows of small branches or sun flecks. Overall the measurements exhibited a clear pattern of a high frequency of fully shaded sensors close to the minimum and a high frequency of fully sunlit values close to the maximum of each time step respectively, with values in between scattered sparsely. These patterns correspond closely to the reference data from the Deutscher Wetterdienst (2024) (Figure 13b), with shaded values closely resembling the pattern of diffuse radiation and fully sunlit values following the global radiation.

### 3.4.2 DART Simulations

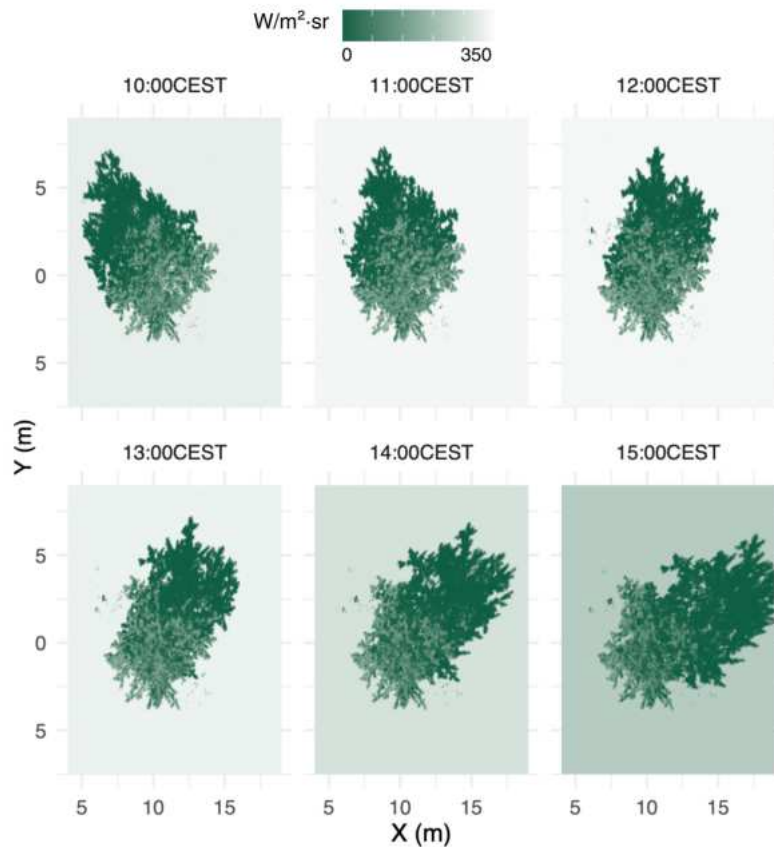


**Figure 14:** DART Nadir radiance images from six time steps of the scene utilising explicit geometries for both wood and foliage. The x and y-axis refer to DART scene coordinates.

Radiative transfer was simulated for all three scenes from 12:10 to 17:10 in 10-minute intervals, resulting in a total of 30 sun positions and 90 simulations. The simulations of all scenes captured the variations in irradiance due to changes in solar angle and tree shading. Figure 14 displays nadir radiance sensor images (the default DART product) of the explicit geometry scene taken throughout the day, highlighting the movement of shadows during the measurement period. These simulated sensor images demonstrate the high spatial resolution of the simulation, clearly showing the shadows cast by individual branches on the ground, as well as small sun flecks in the gaps between the shadows of outer branches and areas with sparse canopy coverage. Figure 15 presents a comparison of nadir radiance sensor images of all three scene types, showcasing resulting differences in the resolution of the shadow cast by the tree model. A clear loss of contrast and detail is visible.

In all 90 simulations, the 72 PAR sensors were simulated, resulting in 2160 simulated PAR measurements for each of the three scenes. A subset of simulated sensor values over the measurement period for all three scenes is shown in Figure 16. A complete overview of all measured and simulated sensor values is given in the Appendix B.

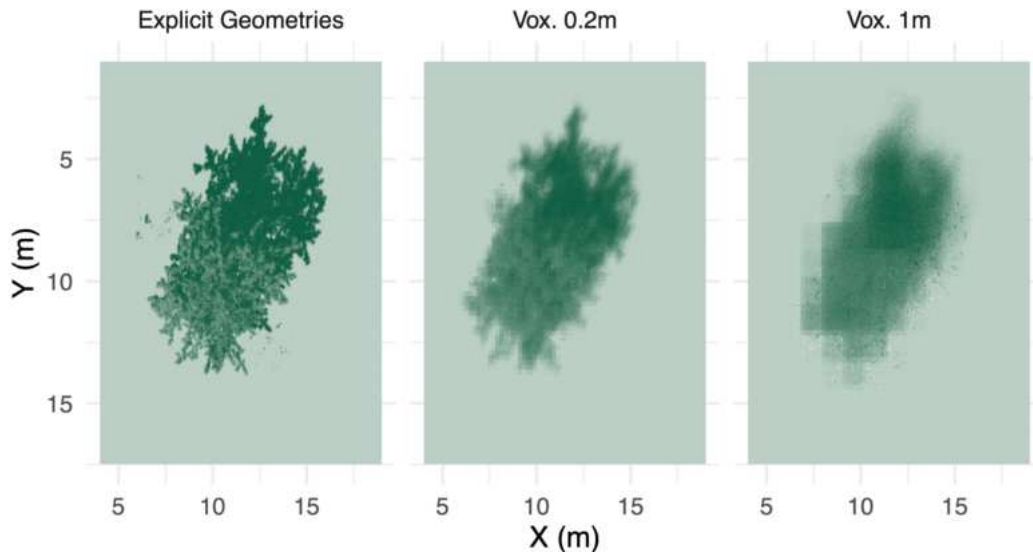


**Figure 15:** Comparison of DART Nadir radiance images of all three scene types at 13:00CEST. The X and Y-axis refer to DART scene coordinates.

### 3.4.3 Validation

#### Temporal Dynamics

Figure 14 presents the time series of measured and predicted PAR values of all three scenes for 24 of the 72 quantum sensor positions across six loggers. Across the majority of sensor positions, the simulated PAR values align well with the measured values, showing similar trends and fluctuations throughout the day. Especially for sensor positions that were never shaded (e.g. Logger 2: sensor 6) the simulated radiation patterns align almost perfectly with the measured values for all three scenes. The predictions from the scene with reconstructed explicit geometries consistently align well with the measured PAR values (e.g. Logger 3: sensor 3; Logger 5: sensor 7; Logger 4: sensor 7), effectively capturing observed trends across various sensor positions. The voxel simulations also provide a good match with the general trends, with the 0.2 m resolution offering a seemingly improved fit compared to the 1 m voxel scene. However, in some cases, the voxel-base simulations fail to capture rapid fluctuations of radiation and exhibit a much more smoothed pattern compared to the measured values and explicit geometries simulations. For example Logger 2: sensor 3 shows a clear sudden drop in radiation in the measured values, with the explicit geometries scene following this drop closely, while the voxel simulations deviate in capturing the troughs. In some cases (e.g. Logger 6: sensor 7) all scene types highly overestimated PAR values, only slightly resembling the overall trend in radiation. Generally, the absolute values of shaded sensors seem to be comparatively higher for the simulated PAR from all scenes, whereas fully sunlit values reside within the same value range as the in-situ measurements.

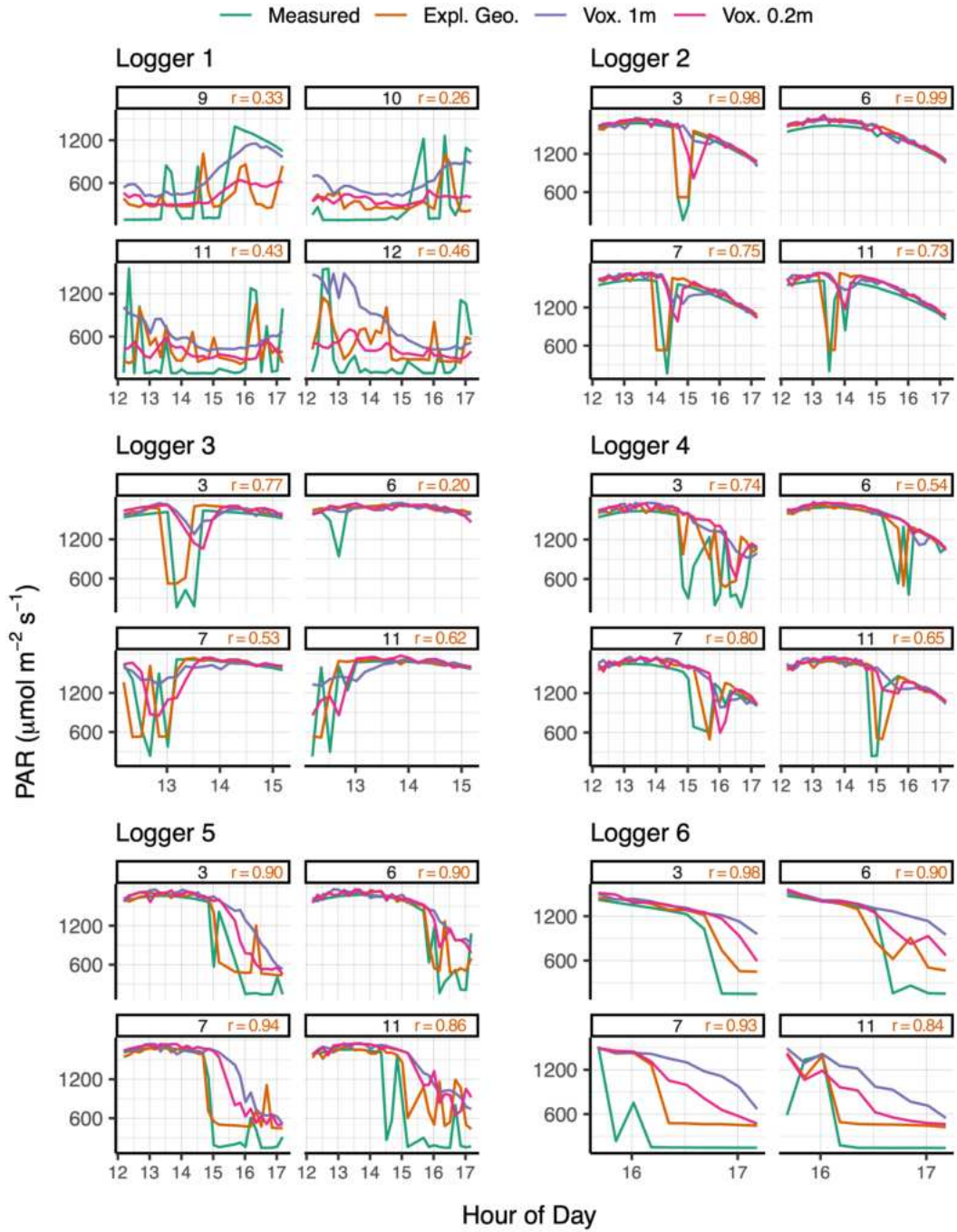


**Figure 16:** Time series of measured and simulated PAR values (explicit geometries, 1 m voxels, 0.2 m voxels) for 24 of the 72 quantum sensor positions over 6 Loggers. Orange  $r$  values refer to the correlation of simulated values from the explicit geometries scene and measured values of each sensor position.

**Table 3:** Summary statistics of per sensor Pearson correlation coefficients for simulated vs. measured PAR values from all three DART scenes.

	Explicit	0.2 m Voxels	1 m Voxels
Mean	0.72	0.62	0.61
Standard Deviation	$\pm 0.28$	$\pm 0.32$	$\pm 0.33$
Maximum	0.99	0.99	0.99
Minimum	-0.30	-0.36	-0.35

### Correlation

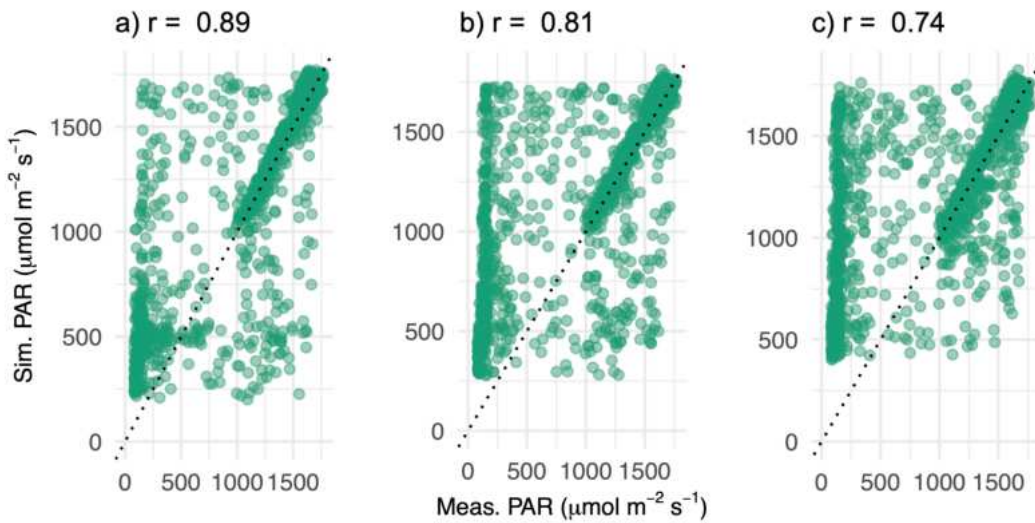


**Figure 17:** Simulated vs. measured PAR scatterplot for each scene respectively. The dotted line is a 1:1 reference line. a) explicit geometries of wood and foliage; b) voxelized foliage with 0.2 m voxels; c) voxelized foliage with 1 m voxels

To statistically compare the simulated PAR values from all three DART scenes with the quantum sensor measurements, various correlations were calculated using Pearson's correlation coefficient  $r$ . All correlations were found to be significant at  $p < 0.001$ . Figure 17 shows scatter plots comparing simulated versus measured PAR values of all sensors for the three different DART scenes. All plots indicate a strong positive correlation, with the explicit geometry scene exhibiting the strongest relationship with the measured data ( $r = 0.89$ ) followed by the 0.2 m voxels scene ( $r = 0.81$ ) and then the 1 m voxels scene ( $r = 0.74$ ). The strongest random scattering is visible for the

lowest quartile where especially the voxel-based scenes overestimated the PAR values in many cases. Table 3 summarizes the per-sensor correlation coefficients showing again that overall the explicit geometry scene indicates the closest relationship with the measured values. With over a third of the sensors exhibiting a correlation of  $r > 0.9$ . However, a quarter of all sensors showed a correlation coefficient of  $r < 0.5$  and two sensors even a negative correlation (Logger 1: Sensor 7 with  $r = -0.21$  and Logger 6: Sensor 12 with  $r = -0.31$ ), indicating a very clear misrepresentation of the measurements. Logger 1, which contains the sensors placed directly under the target tree, close to the stem, shows the lowest correlation overall and no clear differences between the three scene types.

### Class Predictions

The classification of the measured data resulted in 64 % classified as sunlit, 22 % as shaded and 14 % as half-shaded. Figure 18 presents the confusion matrices of the in-situ measurements and the simulate PAR values categories of the three different simulated scenes (a: explicit geometries; b: 0.2 m voxels; c: 1 m voxels).

The matrices illustrate the fraction of the reference class that was correctly classified across the measurement categories, with the opacity representing the fraction size. Overall, the simulations demonstrate a high accuracy for the "sunlit" category with a correct classification rate of 92% for explicit the geometry scene, slightly higher than the voxelized foliage scenes at 89% (0.2 m) and 86% (1 m). The "half-shaded" category for the explicit geometry scenes has a correct classification rate of 70%, which is significantly better than for both voxelized scenes, where in both scenes only 54% were classified correctly, particularly with a higher confusion into the "shaded" category. All scenes exhibited a similar low accuracy in regards to shaded measurements, with 17% for both the explicit geometry scene and the 0.2 m voxels. The 1 m voxel scene correctly classified 20% of the reference classes. The confusion was primarily into the half-shaded class for all three scenes.

### 3.5 Computational Efficiency

All point cloud processing, model construction and radiative transfer modeling was run with an AMD Ryzen 9 3950X 16-Core Processor (3.49 GHz) with 128 GB of RAM.

The construction of stem and foliage geometries and subsequent writing to mesh

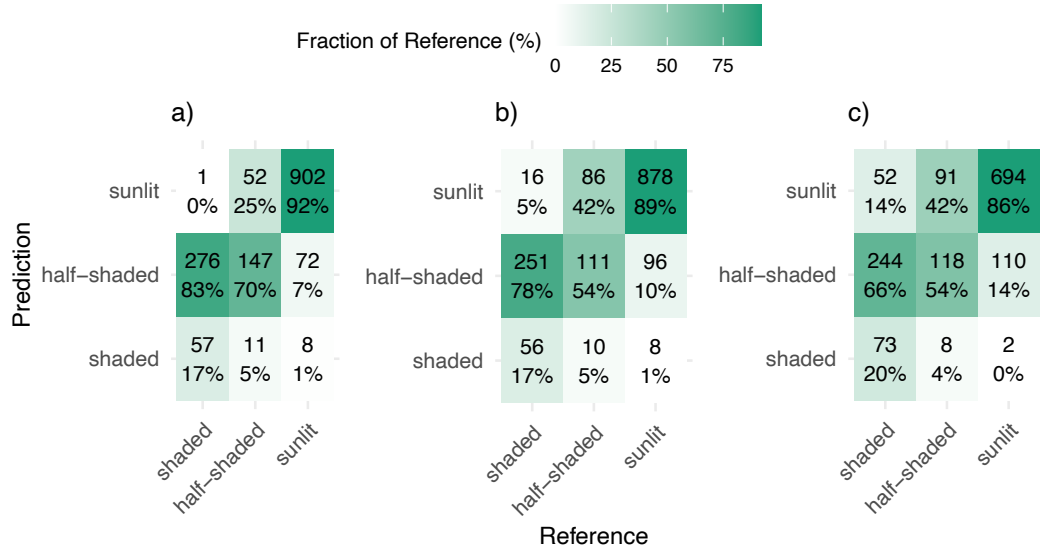


**Figure 18:** Confusion matrices of the in-situ measurements and the predicted categories based on all the three simulated scenes: a) explicit geometries of wood and foliage; b) voxelized foliage with 0.2 m voxels; c) voxelized foliage with 1 m voxels. The category "half-shaded" defines measurements between full shade and full light. The opacity represents the fraction of the reference class that was classified.

files required 59 minutes. Whereas the voxelization took 21 minutes for the 0.2 m voxel size and 8 minutes for the 1 m voxel size. The DART scene featuring explicit geometries for wood and foliage required an average computation time of  $197.17 \pm 8.19$  seconds per time step. In contrast, the scene with turbid foliage voxelized at 0.2 m required an average computation time of  $2433.0 \pm 30.32$  seconds per time step. Each time step for the scene with turbid foliage voxels of 1 m, took  $604.330 \pm 11.22$  seconds.

## 4 Discussion

The primary aim of this thesis was to develop a comprehensive workflow for parameterizing the Discrete Anisotropic Radiative Transfer (DART) model using terrestrial laser scanning (TLS) data. This methodology involves creating reconstructed explicit geometries, validating the simulated results with in-situ measurements, and comparing these results with those obtained from voxel-based approaches, similar to the methods applied by Kükenbrink et al. (2019, 2021) and discussed by Liu et al. (2022). Further, this thesis aims to assess the feasibility of applying this approach to larger spatial scales and accurately quantifying radiative conditions within forest ecosystems.

The findings indicate that the proposed method effectively simulates light extinction through the canopy, offering detailed insights into micro-structural light patterns underneath the target tree. The simulated PAR values from the proposed explicit geometry approach showed a high agreement with in-situ PAR measurements. The explicit geometry scene systematically outperformed voxel-based approaches in both accuracy and computation time. However, for some sensor positions, the simulation displayed inaccurate PAR values and temporal dynamics, showcasing further room for improvement and the necessity for a more detailed parameterization of the RTM.

### 4.1 Simulation Accuracy

The high correlation and close agreement between the simulated sensor values and in-situ measurements for sensor positions that were fully sunlit throughout the measurement period suggest that the parameterization of atmospheric conditions, sun angles, and the atmospheric radiative transfer function in all DART scenes resulted in accurate bottom-of-atmosphere irradiance, precisely representing the overall radiative conditions over the measurement period. The slight variation between the scene types is due to the stochastic nature of the atmospheric radiative transfer model. This accuracy also confirms that the developed approach of formulating PAR sensors within DART as radiance cameras capturing the radiance of a white Lambertian

surface at the actual sensor position and the consequent conversion to PPFD values provides an efficient and accurate solution for simulating punctual PAR measurements in DART. However, due to the sensors averaging radiance over an area of 20 cm<sup>2</sup> they also introduce some uncertainty.

Generally, the results indicate that the shading pattern by the target tree and consequent PAR extinction is simulated correctly. However, shaded PAR values seem to be systematically overestimated, and the proposed approach primarily lacked precision in accurately depicting the variations in PAR in mostly shaded sensor positions. This could have multiple causes. As the optical properties defined for the foliage were averaged values for deciduous leaves, the ratio of transmittance and reflection of the foliage surfaces might not be a realistic representation. Generally, shaded values seem to be overestimated by the simulation, which is clear when comparing the minimum values per sensor over the measurement period. The confusion matrix indicates the same trend, with the fully shaded classes being falsely classified as half-shaded at very high rates. Likely, the transmission by leaf surfaces or voxels was too high, not shading the simulated sensors enough. To address this issue, species-specific optical properties should be applied in the simulation. Kükenbrink et al. (2019) for example gathered optical properties of 20 leaves of the target tree using field spectroradiometers, measuring the spectral response of each tree. Implementing these field measurements in the DART simulation would likely increase the accuracy of the simulation presented here. Additionally, leaf optical properties (LOPs) can vary significantly within the canopy due to factors such as leaf age, position in the crown, and exposure to light. Ideally, multiple samples should be taken at various heights, and the optical properties should be applied based on their vertical and horizontal positions within the crown (Gara et al., 2018). Nevertheless, Kükenbrink et al. (2021) compared their simulations using measured LOPs with those using literature values and found the deviations to be within an acceptable range. This suggests that while precise LOP measurements are preferable, averaged values from literature can still produce reliable results.

Another reason for the overestimation of shaded values could be the amount of diffuse radiation caused by the simulation of the atmosphere. Although the modeled irradiance of sunlit surfaces was shown to be accurate, the overestimation of diffuse radiation could result in inaccuracies in shaded areas. If the atmosphere model overestimates the concentration or scattering effect of aerosols, it can lead to an inflated amount of diffuse radiation reaching shaded areas. Instead of applying standard gas models, a more precise parameterization of atmospheric variables which are input

into the MODTRAN module within DART, utilizing the reference radiation data from the DWD, would likely yield an increase in accuracy (Berk et al., 2014).

The relatively low correlation coefficients for sensor positions that were mostly shaded throughout the measurement period were possibly impacted by sensor noise and disturbances from the natural environment, such as insects or birds. Due to the lower overall variance of these sensors, even minor fluctuations had a disproportionately strong impact on the correlation results. Further, branch or leaf movement which the simulations could not account for, could have also had an effect by causing sunflecks or small-scale shading.

Instead of applying a Digital Elevation Model (DEM) to represent the study area's ground, this approach used a flat terrain to improve computational efficiency. Slope and minor undulations are not represented in the simulation. This could have led to small inaccuracies, as the ground below the target tree was not perfectly even, potentially skewing the positions of the simulated sensors. Additionally, the selected ground optical property may not realistically represent the actual ground optical properties of the study area. However, the impact of ground reflectance and the subsequent reflection of light from the target tree is likely minimal.

Radiation in the simulated DART scenes was defined as a single band in the PAR domain (400-700 nm). Using only a single band can be inaccurate since DART computes average spectral response values for surfaces, turbid volumes, and atmosphere interactions (Gastellu-Etchegorry et al., 2015). A higher accuracy could be achieved by defining narrow spectral bands across the PAR domain. However, this approach would significantly increase the computation time, as the radiative transfer calculations would need to be performed separately for each band.

A further cause of uncertainty in the applied workflow is the classification of wood and foliage. As the point cloud did not exhibit a clear bimodal reflectance distribution, it is uncertain if the threshold of -5.4 dB precisely differentiates wood and leaves. Although visually the classification seemed to be accurate, this confirmation is not precise and likely a fraction of points were misclassified.

One crucial aspect that has not been addressed is the sensitivity of the simulation outcomes to the various input parameters used. Conducting a sensitivity analysis of the methodology would provide valuable insights into how specific parameters for geometry reconstruction (e.g. single point polygon shape, voxel and buffer size) and RTM (e.g. atmospheric conditions or optical properties) influence the simulation results. This analysis would help in identifying the key factors that significantly effect simulation accuracy, guiding further adjustments.

## 4.2 Validation Data

Although the in-situ measurement campaign was extensive, with 60 sensors collecting data over 5 hours, further improvements could strengthen the validation of the simulation. Increased spatial coverage by positioning sensors at different canopy heights and extending the temporal coverage to capture measurements across different seasons and weather conditions. Since the validation measurements in this thesis were only taken during clear conditions, it is uncertain if the same simulation accuracy would be achieved under overcast conditions with highly diffuse radiation. Further, increasing the measured spectral range using spectroradiometers, as applied by Kükenbrink et al. (2019), would yield insights into the spectral variability of light conditions within the canopy, enhancing the overall accuracy and comprehensiveness of the validation process. However, using spectroradiometer measurements also presents various logistical limitations.

## 4.3 Comparison with Other Approaches

Only a few studies have extensively validated their approach for parameterizing an RTM with TLS data. Validation is often bypassed because it can be a tedious process that requires extensive data collection over a large area. Directly comparing accuracy with other validation approaches is difficult, especially when studies have been conducted at different temporal or spatial scales and have used differing approaches for measuring in-situ validation data. Kükenbrink et al. (2019) conducted irradiance measurements using field spectroradiometers to collect reflected radiance data from a white spectralon panel. Their measurements were taken at a sunlit reference location and along various transects within the tree's shadow, using a sled and gimbal system. This method does not capture the diurnal variations at multiple positions. However, similar voxel-based approaches at two voxel sizes (0.2 m and 1 m) were also applied in this thesis. The comparison of the simulation results from all three scenes, as expected, showed higher overall accuracy for the reconstructed explicit geometries in simulating PAR conditions underneath the target tree compared to the voxelized approaches. The voxel-based scenes all exhibited smoother patterns during the measurement period, not reflecting the drastic drops or increases in PAR caused by small-scale shading or sunflecks. This is because the voxels represent foliage as a homogeneous turbid medium, resulting in the loss of clear edges and strong contrasts, especially at larger voxel sizes. The difference between the three scenes is most evident when comparing overall correlation coefficients. However, when investigating the correlation

coefficients for each sensor separately, the differences between the scenes become less pronounced, with the explicit geometry scene only outperforming the 0.2m voxel scene by an average  $r$  difference of 0.11. For four of the 72 sensors, the voxel approaches even showed a higher correlation coefficient than the explicit geometries. The exact reason for this is unclear. Generally, explicit geometries improve the simulation accuracy by avoiding the spatial uncertainties introduced by voxelized approaches, they also have certain drawbacks under specific circumstances. As with all remote sensing approaches, limited coverage and resolution due to large distances from the scanner will produce occlusion effects in the gathered data (Cifuentes et al., 2017). With the proposed approach reconstructing geometries directly from the point cloud, these occlusion effects might be more strongly pronounced compared to a voxelized foliage approach with larger voxel sizes. Nevertheless, possible occlusion effects will also influence the PAD calculation in voxel-based approaches, which can lead to inaccuracies. However, this can partially be addressed by calibrating the distance weighting when calculating PAD.

The results align with Liu et al. (2022), who compared a 3D-explicit approach with a voxelized version of the same 3D models. Their DART simulations also found significant deviations from the explicit geometry approach in voxel-based simulations, especially with larger voxel sizes. However, the results regarding simulation run-time are only partially aligned. My results showed that the DART model with explicit geometries required significantly less computation time compared to voxel-based methods. For the 0.2 m voxels, the computation time increased by a factor of 12, and for the 1 m voxels, it increased by a factor of 3. Similarly, (Liu et al., 2022) found that voxel-based simulations with very small voxel sizes were highly resource-intensive, however, larger voxel sizes (1-2 m) improved computational efficiency, requiring less time and resources than their 3D-explicit models, which was not true for my simulations. It is important to note that in the voxel scenes implemented in this thesis, the branch stem and branches were still represented as explicit geometries whereas Liu et al. (2022) used a fully voxelized approach for their comparison.

Further, as the applied workflow did not utilize the DART `sequence`-module, the computation time for the voxelized approach might be inflated compared to other studies. This module optimizes computation time by only calculating the necessary variables per sequence step and copying pre-calculated parameters or files. This thesis did not use this due to compatibility issues with the sensor simulation setup. As a result, for every simulation iteration, the voxel file was read, and polygons describing the voxel shape were written, leading to increased computation time.

These comparisons of runtime do not include the generation of the tree models, which is an important factor to consider. Constructing the explicit geometries requires substantial computational resources and processing time. For larger scales, the difference in computation time between explicit geometries and voxel-based approaches will become more pronounced. When applying radiative transfer models (RTM) at a large scale, the efficiency of polygon creation would need to be greatly improved to be feasible.

Compared to the approach developed by Calders et al. (2018), the voxel-based polygon reconstruction method (Frey et al., 2024) provides various advantages. The latter does not require any manual adjustment of parameters or the availability of leaf-off scans for the creation of the tree models, making it more versatile and less labor-intensive. Additionally, the method employed in this thesis is likely more applicable to lower resolution TLS data, as it is not as prone to failing and strongly misrepresenting canopy structure as QSMs that often require high-quality scans (Morhart et al., 2024). The developed methodology to replicate PAR sensors at exact positions within the DART scene was shown to be accurate and computationally efficient. Comparatively, the method utilized by Kükenbrink et al. (2019, 2021), which employed the Radiative Budget tool within DART to extract irradiance values, is computationally very intensive, as it calculates the incoming and outgoing radiation as well as the fractions of scattered, intercepted and absorbed radiation. This is particularly true when using DART-Lux mode, although a future improvement of this functionality for DART-Lux has been announced. Further, the Radiative Budget tool provides voxel-based values and can therefore introduce spatial uncertainties, whereas the precise definition of the virtual sensor positions is not limited by resolution. While, the Radiative Budget tool is beneficial for generating comprehensive 3D irradiance profiles, which are useful for detailed investigations of light interactions within forest canopies, its computational inefficiency makes it less suitable for validation purposes.

## 4.4 Implications and Limitations

The results demonstrate that accurate reconstruction of forest structures using TLS data enables precise simulations of light extinction by the canopy, which is essential for understanding the dynamics of light availability that directly influence photosynthesis, evapotranspiration, and phenology (Sage and Kubien, 2007; Kull and Kruijt, 1998; Canham et al., 1990; Van der Zande et al., 2010; Caffarra and Donnelly, 2011).

Although some inaccuracies persist, further improvements in the parameterization of DART scenes can enhance this methodology, making it a powerful tool for quantifying radiative conditions in forest ecosystems. This advancement holds significant potential for applications in silvicultural management, research, and remote sensing.

When applied at the stand level rather than to a single target tree, new opportunities for ecophysiological research arise. By quantifying even microstructural light patterns, the proposed method allows for a nuanced understanding of PAR availability within forest stands and the consequent predictions on various ecological processes, such as species interactions, under-story growth, and forest succession processes (Forrester et al., 2019; Leuchner et al., 2012; De Pauw et al., 2022). The high resolution of retrieved light extinction patterns allows to study the impact on forest microclimates and the associated effects on flora and fauna, providing a more detailed insight into ecosystem functioning than is possible using traditional measurement methods or more simplistic radiative transfer models such as one-dimensional light extinction, voxel-based methods or generalized geometric crown models (Calders et al., 2018; Liu et al., 2022; Van der Zande et al., 2011; Ligot et al., 2014).

When applying this method to wider spectral ranges, these simulations of light conditions can be used as a reference point for calibrating remote sensing data, thereby improving the precision of vegetation indices and other remote sensing products (Ferreira et al., 2018; Wang et al., 2018). As demonstrated by Kükenbrink et al. (2019), simplifying canopy structure can lead to significant errors when calculating vegetation indices based on top-of-canopy reflectance. The approach proposed in this study shows improved performance and accuracy compared to their voxel-based approach, suggesting an even higher potential for accurate and efficient modeling of canopy light interactions. This advancement can subsequently enhance the reliability of remote-sensing products. However, for this calibration of remote sensing applications, deployment at larger scales, such as at the forest stand level, would be necessary (Ferreira et al., 2018). Here, the proposed method may encounter limitations. Further testing at larger scales is needed to determine the feasibility of using these highly detailed tree reconstructions with complex geometries and a large number of faces. Optimization for computational efficiency will likely be necessary. One approach could be to reduce the number of surfaces created, perhaps by combining polygons and consequently creating smoother, continuous surfaces for the stems. Algorithms for topology optimization similar to those utilized in industrial design or 3D printing could be utilized here (Bacciaglia et al., 2021). Since DART calculates radiative interactions for each polygon face, the reduction of faces representing larger, continu-

ous surfaces, such as the stem or large branches, could decrease computation time without significantly sacrificing accuracy.

Additionally, there are considerable differences in leaf morphology both within and between species. Since this geometry reconstruction approach has only been tested on a single species so far, further research is needed to validate its applicability across different species with varied leaf shapes and orientations. This could potentially address the limitations of representing the wide range of leaf appearances and provide the opportunity to apply large-scale RTMs across heterogeneous forest environments. For larger-scale approaches, semi-automation of the proposed method would be necessary. Currently, the process of creating tree models, parameterizing the DART scenes, and subsequently extracting the DART products relies on multiple separate scripts and notebooks. Optimizing this process could involve developing a bash script to integrate point cloud processing and the RTM. This would streamline the workflow, requiring the user to only provide the point cloud and a metadata file with relevant information to simulate radiative transfer based on LiDAR point clouds.

## 4.5 Future Research

In addition to addressing the limitations and potential inaccuracies of the applied methodology discussed in the previous sections, there is significant room for improvement and expansion of the functionalities of LiDAR-based RTM applications. In the following, I will outline some areas where future research should focus.

As TLS-based approaches often suffer from occlusion issues in the upper canopy, which this approach cannot account for, the integration of unmanned aerial vehicle (UAV) based LiDAR could provide a great addition to furthering the accuracy of RTMs parameterized by LiDAR. Although TLS currently provides higher resolutions and accuracy, UAV-based LiDAR is not only more cost-effective but also easier to deploy. With the technology's ongoing improvements in accuracy, resolution and ease of use, UAV-based LiDAR will likely become quicker, easier, and more economical to use (Hu et al., 2020; Dainelli et al., 2021).

Although machine learning (ML) methods for point cloud processing, such as segmentation, species classification, and wood and foliage classification are already in use (e.g. Li et al. (2023); Jiang et al. (2023); Liu et al. (2021)), there is significant potential for further development and use of machine learning implementations, especially in regards to surface reconstruction and tree model creation. With the increasing

availability of realistic 3D models of different tree species (e.g. The Grove 3D (2024)) and various software solutions for simulating TLS or UAV-based LiDAR scanning (Manivasagam et al., 2020), new opportunities are emerging for the development of machine-learning algorithms which derive canopy structure from LiDAR data. The need to collect real-world training data, which would be extremely labor-intensive in this context, is becoming obsolete, creating the opportunity to extensively train ML-based point cloud completion and geometry reconstruction algorithms (similar to Liu et al. (2020) or Adams and Elhabian (2024)), potentially producing more accurate results and combating occlusion effects that lead to fragmented or incorrect surfaces. The static 3D representations of forest canopies used in this research effectively simulate light distribution and radiative transfer. Although precisely representing the variations on the day of data collection, they do not fully capture the dynamic aspects of light within tree canopies. Various factors, such as seasonal changes, the weight of branches, and environmental conditions, significantly affect canopy structure over time. For instance, leaf phenology, from emergence to eventual senescence alters the distribution and density of foliage, impacting light penetration and shading patterns (Huang et al., 2018; Jin et al., 2024). Additionally, branches can shift due to their weight or external influences like wind, further modifying the canopy's architecture (Sheppard et al., 2017). Future research might aim to develop dynamic 3D tree models that integrate these temporal variations. Such models would offer a more precise depiction of how trees interact with their surroundings throughout different periods. Although likely challenging to implement, these models could yield valuable insights into the evolving light conditions within forests. On the contrary, greatly increasing the 3D model complexity and therefore also computational demands may only result in marginal accuracy improvements. Such approaches might only become practical in the future with the advent of more powerful computing tools.

## 5 Conclusion

In conclusion, this thesis presents a methodology for parameterizing the DART model using explicit geometries derived from TLS data to simulate PAR values at specified sensor positions. The simulated values were validated against in-situ measurements and compared to voxel-based approaches. The primary findings indicate that utilizing explicit geometry tree models in RTMs provides an accurate tool for simulating light extinction through forest canopies. The results demonstrate a high correlation between simulated and measured PAR values and showcase the superiority of explicit geometries over voxel-based methods in terms of accuracy and computational efficiency. The proposed approach accurately represents small-scale dynamics of light extinction underneath the target tree, offering detailed insights into micro-structural shading patterns. While some inaccuracies persist, these can likely be addressed through more detailed parameterization of the DART scene, including a detailed DEM, accurate leaf optical properties, and more precise atmospheric parameters.

Future research should focus on validating this methodology across various forest types, considering seasonal variations and diverse environmental conditions to enhance simulation robustness and applicability. Additionally, integrating other remote sensing technologies, such as UAV-based LiDAR, could significantly expand the spatial coverage and resolution of the data, facilitating more comprehensive ecological studies and forest management practices. Incorporating machine learning algorithms in the 3D tree model generation and developing dynamic models that account for environmental factors and phenology hold great potential for further increasing simulation accuracy and robustness. These advancements could improve the precision of ecological and radiative transfer models, contributing to large-scale ecological or climate science studies, sustainable forest management, and enhanced remote sensing products. By addressing these future research directions and utilizing emerging technologies, the proposed method can become a powerful tool for accurately quantifying radiative conditions in forest ecosystems.

## 6 Acknowledgments

I would like to thank everyone who helped me with this work. First and foremost, many thanks to Dr. Julian Frey, who was always there for me, providing confidence, assistance and excitement whenever needed. His support and availability were incredibly valuable throughout the entire process. I would also like to thank Prof. Dr. Teja Kattenborn for taking on the role of the second examiner.

Special thanks to Nicolas Lauret and Jean-Philippe Gastellu-Etchegorry from the DART team for answering my questions and offering their expertise. Additionally, I appreciate the suggestions provided by Dr. Anna Göritz.

I also acknowledge the assistance of AI tools like ChatGPT, which were utilized in helping with code development and restructuring during the writing process.

Anschliesend, auch vielen Dank an alle meine lieben Freunde, die immer für mich da waren und aus Solidarität mit mir in die Mensa gehen, auch wenn sie gar nicht mehr an der Uni sind. Danke an Mama und Papa für die ganze Unterstützung in den letzten Jahren. Jetzt hab ichs auch geschafft.

# Bibliography

Adams, J. and Elhabian, S. (2024). Point2ssm++: Self-supervised learning of anatomical shape models from point clouds. *arXiv preprint arXiv:2405.09707*.

Anderson, M. C. (1964). Studies of the woodland light climate: I. the photographic computation of light conditions. *The Journal of Ecology*, pages 27–41.

Ashton, P. S. (1958). Light intensity measurements in rain forest near santarem, brazil. *The Journal of Ecology*, pages 65–70.

Bacciaglia, A., Ceruti, A., and Liverani, A. (2021). Surface smoothing for topological optimized 3d models. *Structural and Multidisciplinary Optimization*, 64(6):3453–3472.

Baldocchi, D., Falge, E., Gu, L., Olson, R., Hollinger, D., Running, S., Anthoni, P., Bernhofer, C., Davis, K., Evans, R., et al. (2001). Fluxnet: A new tool to study the temporal and spatial variability of ecosystem-scale carbon dioxide, water vapor, and energy flux densities. *Bulletin of the American Meteorological Society*, 82(11):2415–2434.

Berk, A., Anderson, G. P., Acharya, P. K., Bernstein, L. S., Cooley, T. W., Shettle, E. P., and Robertson, D. C. (2014). Modtran6: A major upgrade of the modtran radiative transfer code. In *Proceedings of SPIE - The International Society for Optical Engineering*, volume 9088, page 90880H.

Berk, A., Bernstein, L. S., Robertson, D. C., et al. (1989). Modtran: A moderate resolution model for lowtran 7.

Blender Development Team (2024). Blender.

Braghieri, R. K., Quaife, T., Black, E., Ryu, Y., Chen, Q., De Kauwe, M. G., and Baldocchi, D. (2020). Influence of sun zenith angle on canopy clumping and the resulting impacts on photosynthesis. *Agricultural and Forest Meteorology*, 291:108065.

Brown, N., Jennings, S., Wheeler, P., and Nabe-Nielsen, J. (2000). An improved method for the rapid assessment of forest understorey light environments. *Journal of Applied Ecology*, 37(6):1044–1053.

Caffarra, A. and Donnelly, A. (2011). The ecological significance of phenology in four different tree species: effects of light and temperature on bud burst. *International journal of Biometeorology*, 55:711–721.

Calders, K., Origo, N., Burt, A., Disney, M., Nightingale, J., Raumonen, P., Åkerblom, M., Malhi, Y., and Lewis, P. (2018). Realistic forest stand reconstruction from terrestrial lidar for radiative transfer modelling. *Remote Sensing*, 10(6):933.

Canham, C. D., Denslow, J. S., Platt, W. J., Runkle, J. R., Spies, T. A., and White, P. S. (1990). Light regimes beneath closed canopies and tree-fall gaps in temperate and tropical forests. *Canadian journal of forest research*, 20(5):620–631.

Caya, M. V. C., Alcantara, J. T., Carlos, J. S., and Cereno, S. S. B. (2018). Photosynthetically active radiation (par) sensor using an array of light sensors with the integration of data logging for agricultural application. In *2018 3rd International Conference on Computer and Communication Systems (ICCCS)*, pages 377–381. IEEE.

Cescatti, A. (1997). Modelling the radiative transfer in discontinuous canopies of asymmetric crowns. i. model structure and algorithms. *Ecological Modelling*, 101(2):263–274.

Cifuentes, R., Van der Zande, D., Salas, C., Tits, L., Farifteh, J., and Coppin, P. (2017). Modeling 3d canopy structure and transmitted par using terrestrial lidar. *Canadian Journal of Remote Sensing*, 43(2):124–139.

Cignoni, P., Callieri, M., Corsini, M., Dellepiane, M., Ganovelli, F., and Ranzuglia, G. (2008). Meshlab: an open-source mesh processing tool. <http://meshlab.sourceforge.net>. Accessed: 2024-06-28.

CloudCompare (version 2.11.3) (2023). Cloudcompare (version 2.x) [gpl software]. <http://www.cloudcompare.org/>. Retrieved from <http://www.cloudcompare.org/>.

Da Silva, D., Balandier, P., Boudon, F., Marquier, A., and Godin, C. (2012). Modeling of light transmission under heterogeneous forest canopy: an appraisal of the effect of the precision level of crown description. *Annals of forest science*, 69:181–193.

Dainelli, R., Toscano, P., Di Gennaro, S. F., and Matese, A. (2021). Recent advances in unmanned aerial vehicles forest remote sensing—a systematic review. part ii: Research applications. *Forests*, 12(4):397.

Damm, A., Paul [U+2010] Limoges, E., Kükenbrink, D., Bachofen, C., and Morsdorf, F. (2020). Remote sensing of forest gas exchange: Considerations derived from a tomographic perspective. *Global Change Biology*, 26(4):2717–2727.

Danner, M., Locherer, M., Hank, T., Richter, K., Consortium, E., et al. (2015). Measuring leaf area index (lai) with the li-cor lai 2200c or lai-2200 (+ 2200clear kit)—theory, measurement, problems, interpretation.

Danson, F. M., Disney, M. I., Gaulton, R., Schaaf, C., and Strahler, A. (2018). The terrestrial laser scanning revolution in forest ecology. *Interface Focus*, 8(2):20180001.

de Boissieu, F., Chraibi, E., Lavalle, C., and Féret, J. (2019). pytools4dart: Python api to dart radiative transfer simulator.

de León, M. A. P. and Bailey, B. N. (2019). Evaluating the use of beer's law for estimating light interception in canopy architectures with varying heterogeneity and anisotropy. *Ecological Modelling*, 406:133–143.

De Pauw, K., Sanczuk, P., Meeussen, C., Depauw, L., De Lombaerde, E., Govaert, S., Vanneste, T., Brunet, J., Cousins, S. A., Gasperini, C., et al. (2022). Forest understorey communities respond strongly to light in interaction with forest structure, but not to microclimate warming. *New Phytologist*, 233(1):219–235.

dos Reis, M. G. and Ribeiro, A. (2020). Conversion factors and general equations applied in agricultural and forest meteorology. *Agrometeoros*, 27(2).

Ferment, A., Picard, N., Gourlet-Fleury, S., and Baraloto, C. (2001). A comparison of five indirect methods for characterizing the light environment in a tropical forest. *Annals of forest science*, 58(8):877–891.

Ferreira, M. P., Féret, J.-B., Grau, E., Gastellu-Etchegorry, J.-P., Do Amaral, C. H., Shimabukuro, Y. E., and de Souza Filho, C. R. (2018). Retrieving structural and chemical properties of individual tree crowns in a highly diverse tropical forest with 3d radiative transfer modeling and imaging spectroscopy. *Remote sensing of environment*, 211:276–291.

Forrester, D. I., Rodenfels, P., Haase, J., Härdtle, W., Leppert, K. N., Niklaus, P. A., von Oheimb, G., Scherer-Lorenzen, M., and Bauhus, J. (2019). Tree-species interactions increase light absorption and growth in chinese subtropical mixed-species plantations. *Oecologia*, 191(2):421–432.

Frazer, G. W., Canham, C. D., and Lertzman, K. P. (1999). Gap light analyzer (gla), version 2.0: Imaging software to extract canopy structure and gap light transmission indices from true-colour fisheye photographs, users manual and program documentation. *Simon Fraser University, Burnaby, British Columbia, and the Institute of Ecosystem Studies, Millbrook, New York*, 36.

Frey, J., Schindler, Z., Morhart, C., Larysch, E., and Seifert, T. (2024). Terrestrial-laser-scanning-based reconstruction of a tree's wood and leaves for radiative transfer modelling. Chair of Forest Growth and Dendroecology, University of Freiburg, Freiburg im Breisgau, Germany; Department of Forest and Wood Science, Stellenbosch University, Matieland, South Africa. Draft.

Gara, T. W., Darvishzadeh, R., Skidmore, A. K., and Wang, T. (2018). Impact of vertical canopy position on leaf spectral properties and traits across multiple species. *Remote sensing*, 10(2):346.

Gastellu-Etchegorry, J.-P., Yin, T., Lauret, N., Cajgfinger, T., Gregoire, T., Grau, E., Feret, J.-B., Lopes, M., Guilleux, J., Dedieu, G., et al. (2015). Discrete anisotropic radiative transfer (dart 5) for modeling airborne and satellite spectroradiometer and lidar acquisitions of natural and urban landscapes. *Remote Sensing*, 7(2):1667–1701.

Gersonde, R., Battles, J. J., and O'Hara, K. L. (2004). Characterizing the light environment in sierra nevada mixed-conifer forests using a spatially explicit light model. *Canadian Journal of Forest Research*, 34(6):1332–1342.

Gleason, K. E., Nolin, A. W., and Roth, T. R. (2013). Charred forests increase snowmelt: Effects of burned woody debris and incoming solar radiation on snow ablation. *Geophysical Research Letters*, 40(17):4654–4661.

Govaerts, Y. M. and Verstraete, M. M. (1998). Raytran: A monte carlo ray-tracing model to compute light scattering in three-dimensional heterogeneous media. *IEEE Transactions on geoscience and remote sensing*, 36(2):493–505.

Hackenberg, J., Spiecker, H., Calders, K., Disney, M., and Raumonen, P. (2015). Simpletree —an efficient open source tool to build tree models from tls clouds. *Forests*, 6(12):4245–4294.

Hale, S. E., Edwards, C., Mason, W., Price, M., and Peace, A. (2009). Relationships between canopy transmittance and stand parameters in sitka spruce and scots pine stands in britain. *Forestry*, 82(5):503–513.

Hu, T., Sun, X., Su, Y., Guan, H., Sun, Q., Kelly, M., and Guo, Q. (2020). Development and performance evaluation of a very low-cost uav-lidar system for forestry applications. *Remote Sensing*, 13(1):77.

Huang, H. M., Dong, R., He, D. N., Xiang, Y. R., Zhang, X. J., Chen, J., and Tao, J. P. (2018). Effects of temporal and spatial variation of canopy structures and light conditions on population characteristics of fargesia decurvata. *Ying yong sheng tai xue bao= The journal of applied ecology*, 29(7):2129–2138.

Jennings, S., Brown, N., and Sheil, D. (1999). Assessing forest canopies and understorey illumination: canopy closure, canopy cover and other measures. *Forestry*, 72(1):59–74.

Jiang, T., Zhang, Q., Liu, S., Liang, C., Dai, L., Zhang, Z., Sun, J., and Wang, Y. (2023). Lwsnet: A point-based segmentation network for leaf-wood separation of individual trees. *Forests*, 14(7):1303.

Jin, P., Xu, M., Yang, Q., and Zhang, J. (2024). The influence of stand composition and season on canopy structure and understory light environment in different subtropical montane pinus massoniana forests. *PeerJ*, 12:e17067.

Jogireddy, V. R., Cox, P. M., Huntingford, C., Harding, R. J., and Mercado, L. (2006). An improved description of canopy light interception for use in a gcm land-surface scheme: calibration and testing against carbon fluxes at a coniferous forest.

Kluyver, T., Ragan-Kelley, B., Pérez, F., Granger, B., Bussonnier, M., Frederic, J., Kelley, K., Hamrick, J., Grout, J., Corlay, S., Ivanov, P., Avila, D., Abdalla, S., and Willing, C. (2016). Project jupyter. Accessed: 2024-06-25.

Kükenbrink, D., Hueni, A., Schneider, F. D., Damm, A., Gastellu-Etchegorry, J.-P., Schaepman, M. E., and Morsdorf, F. (2019). Mapping the irradiance field of a single tree: Quantifying vegetation-induced adjacency effects. *IEEE Transactions on Geoscience and Remote Sensing*, 57(7):4994–5011.

Kükenbrink, D., Schneider, F. D., Schmid, B., Gastellu-Etchegorry, J.-P., Schaepman, M. E., and Morsdorf, F. (2021). Modelling of three-dimensional, diurnal

light extinction in two contrasting forests. *Agricultural and Forest Meteorology*, 296:108230.

Kull, O. and Kruijt, B. (1998). Leaf photosynthetic light response: a mechanistic model for scaling photosynthesis to leaves and canopies. *Functional Ecology*, 12(5):767–777.

Leuchner, M., Hertel, C., Rötzer, T., Seifert, T., Weigt, R., Werner, H., and Menzel, A. (2012). *Solar Radiation as a Driver for Growth and Competition in Forest Stands*, page 175–191. Springer Berlin Heidelberg.

Lewis, P. (1999). Three-dimensional plant modelling for remote sensing simulation studies using the botanical plant modelling system. *Agronomie*, 19(3-4):185–210.

Li, J., Liu, J., and Huang, Q. (2023). Pointdmm: A deep-learning-based semantic segmentation method for point clouds in complex forest environments. *Forests*, 14(12):2276.

Li, X. and Strahler, A. H. (1985). Geometric-optical modeling of a conifer forest canopy. *IEEE Transactions on Geoscience and Remote Sensing*, GE-23(5):705–721.

Ligot, G., Balandier, P., Courbaud, B., and Claessens, H. (2014). Forest radiative transfer models: which approach for which application? *Canadian Journal of Forest Research*, 44(5):391–403.

Liu, C., Calders, K., Meunier, F., Gastellu-Etchegorry, J., Nightingale, J., Disney, M., Origo, N., Woodgate, W., and Verbeeck, H. (2022). Implications of 3d forest stand reconstruction methods for radiative transfer modeling: A case study in the temperate deciduous forest. *Journal of Geophysical Research: Atmospheres*, 127(14):e2021JD036175.

Liu, M., Sheng, L., Yang, S., Shao, J., and Hu, S.-M. (2020). Morphing and sampling network for dense point cloud completion. In *Proceedings of the AAAI conference on artificial intelligence*, volume 34, pages 11596–11603.

Liu, S., Zhang, M., Kadam, P., Kuo, C.-C. J., Liu, S., Zhang, M., Kadam, P., and Kuo, C.-C. J. (2021). Explainable machine learning methods for point cloud analysis. *3D Point Cloud Analysis: Traditional, Deep Learning, and Explainable Machine Learning Methods*, pages 87–140.

LuxCoreRender Team (2024). Luxcorerender: A physically based and unbiased rendering engine. <https://luxcorerender.org/>. Accessed: 2024-06-28.

Macfarlane, C., Hoffman, M., Eamus, D., Kerp, N., Higginson, S., McMurtrie, R., and Adams, M. (2007). Estimation of leaf area index in eucalypt forest using digital photography. *Agricultural and forest meteorology*, 143(3-4):176–188.

Manivasagam, S., Wang, S., Wong, K., Zeng, W., Sazanovich, M., Tan, S., Yang, B., Ma, W.-C., and Urtasun, R. (2020). Lidarsim: Realistic lidar simulation by leveraging the real world. In *Proceedings of the IEEE/CVF Conference on Computer Vision and Pattern Recognition*, pages 11167–11176.

Matusz, S. (1953). Photometer for measuring the light transmitted through forest tree crowns.

McElhinny, C., Gibbons, P., Brack, C., and Bauhus, J. (2005). Forest and woodland stand structural complexity: its definition and measurement. *Forest Ecology and Management*, 218(1-3):1–24.

Millard, P. (1996). Ecophysiology of the internal cycling of nitrogen for tree growth. *Zeitschrift für Pflanzenernährung und Bodenkunde*, 159(1):1–10.

Morhart, C., Schindler, Z., Frey, J., Sheppard, J. P., Calders, K., Disney, M., Morsdorf, F., Raumonen, P., and Seifert, T. (2024). Limitations of estimating branch volume from terrestrial laser scanning. *European Journal of Forest Research*, pages 1–16.

Murdoch, D. and Adler, D. (2022). *rgl: 3D Visualization Using OpenGL*. R package version 0.110.2.

Niinemets, U. (2007). Photosynthesis and resource distribution through plant canopies. *Plant, cell & environment*, 30(9):1052–1071.

North, P. R. (1996). Three-dimensional forest light model using a monte carlo method. *IEEE Transactions on Geoscience and Remote Sensing*, 34(2):473–481.

OpenStreetMap (2017). Planet dump retrieved from <https://planet.osm.org> . <https://www.openstreetmap.org>.

Paquette, A., Messier, C., Périnet, P., and Cogliastro, A. (2008). Simulating light availability under different hybrid poplar clones in a mixed intensive plantation system. *Forest Science*, 54(5):481–489.

Parker, G. G., Fitzjarrald, D. R., and Sampaio, I. C. G. (2019). Consequences of environmental heterogeneity for the photosynthetic light environment of a tropical forest. *Agricultural and Forest Meteorology*, 278:107661.

Pharr, M., Jakob, W., and Humphreys, G. (2016). *Physically Based Rendering: From Theory to Implementation*. Morgan Kaufmann.

Pisek, J., Sonnentag, O., Richardson, A. D., and Mõttus, M. (2013). Is the spherical leaf inclination angle distribution a valid assumption for temperate and boreal broadleaf tree species? *Agricultural and Forest Meteorology*, 169:186–194.

Qi, J., Xie, D., Yin, T., Yan, G., Gastellu-Etchegorry, J.-P., Li, L., Zhang, W., Mu, X., and Norford, L. K. (2019). Less: Large-scale remote sensing data and image simulation framework over heterogeneous 3d scenes. *Remote Sensing of Environment*, 221:695–706.

R Core Team (2022). *R: A Language and Environment for Statistical Computing*. R Foundation for Statistical Computing, Vienna, Austria.

Raumonen, P., Kaasalainen, M., Åkerblom, M., Kaasalainen, S., Kaartinen, H., Vastaranta, M., Holopainen, M., Disney, M., and Lewis, P. (2013). Fast automatic precision tree models from terrestrial laser scanner data. *Remote Sensing*, 5(2):491–520.

Restrepo-Coupe, N., da Rocha, H. R., Hutyra, L. R., da Araujo, A. C., Borma, L. S., Christoffersen, B., Cabral, O. M., de Camargo, P. B., Cardoso, F. L., da Costa, A. C. L., et al. (2013). What drives the seasonality of photosynthesis across the amazon basin? a cross-site analysis of eddy flux tower measurements from the brasil flux network. *Agricultural and Forest Meteorology*, 182:128–144.

Ross, J. and Sulev, M. (2000). Sources of errors in measurements of par. *Agricultural and forest meteorology*, 100(2-3):103–125.

Sage, R. F. and Kubien, D. S. (2007). The temperature response of c3 and c4 photosynthesis. *Plant, cell & environment*, 30(9):1086–1106.

Schindler, Z., Larysch, E., Frey, J., Sheppard, J. P., Obladen, N., Kröner, K., Seifert, T., and Morhart, C. (2024). From dawn to dusk: High resolution tree shading model based on terrestrial lidar data. *Remote Sensing*, 1(0). Submitted to Remote Sens. for possible open access publication under the terms and conditions of the Creative Commons Attribution (CC BY) license (<https://creativecommons.org/licenses/by/4.0/>). Draft version.

Sheppard, J., Morhart, C., Hackenberg, J., and Spiecker, H. (2017). Terrestrial laser scanning as a tool for assessing tree growth. *iForest: Biogeosciences and Forestry*, 10(1):172–179.

Stadt, K. J. and Lieffers, V. J. (2000). Mixlight: a flexible light transmission model for mixed-species forest stands. *Agricultural and Forest Meteorology*, 102(4):235–252.

The Grove 3D (2024). The grove - tree simulation. [www.thegrove3d.com](http://www.thegrove3d.com). Accessed: 2024-06-26.

Tinya, F., Mihók, B., Márialigeti, S., Mag, Z., and Ódor, P. (2009). A comparison of three indirect methods for estimating understory light at different spatial scales in temperate mixed forests. *Community Ecology*, 10(1):81–90.

Valladares, F. (2003). Light heterogeneity and plants: from ecophysiology to species coexistence and biodiversity. *Progress in botany: genetics physiology systematics ecology*, pages 439–471.

Van der Zande, D., Stuckens, J., Verstraeten, W. W., Mereu, S., Muys, B., and Coppin, P. (2011). 3d modeling of light interception in heterogeneous forest canopies using ground-based lidar data. *International Journal of Applied Earth Observation and Geoinformation*, 13(5):792–800.

Van der Zande, D., Stuckens, J., Verstraeten, W. W., Muys, B., and Coppin, P. (2010). Assessment of light environment variability in broadleaved forest canopies using terrestrial laser scanning. *Remote Sensing*, 2(6):1564–1574.

Vicari, M. B., Disney, M., Wilkes, P., Burt, A., Calders, K., and Woodgate, W. (2019). Leaf and wood classification framework for terrestrial lidar point clouds. *Methods in Ecology and Evolution*, 10(5):680–694.

Vincent, G., Antin, C., Laurans, M., Heurtebize, J., Durrieu, S., Lavalle, C., and Dauzat, J. (2017). Mapping plant area index of tropical evergreen forest by airborne laser scanning. a cross-validation study using lai2200 optical sensor. *Remote Sensing of Environment*, 198:254–266.

Wang, Y., Kallel, A., Yang, X., Regaieg, O., Lauret, N., Guilleux, J., Chavanon, E., and Gastellu-Etchegorry, J.-P. (2022). Dart-lux: An unbiased and rapid monte carlo radiative transfer method for simulating remote sensing images. *Remote Sensing of Environment*, 274:112973.

Wang, Z., Skidmore, A. K., Darvishzadeh, R., and Wang, T. (2018). Mapping forest canopy nitrogen content by inversion of coupled leaf-canopy radiative transfer models from airborne hyperspectral imagery. *Agricultural and forest meteorology*, 253:247–260.

Webster, C., Rutter, N., Zahner, F., and Jonas, T. (2016). Measurement of incoming radiation below forest canopies: A comparison of different radiometer configurations. *Journal of Hydrometeorology*, 17(3):853–864.

Wetterdienst, D. (2024). Climate data center. Accessed: 2024-04-17.

Widlowski, J.-L., Mio, C., Disney, M., Adams, J., Andredakis, I., Atzberger, C., Brennan, J., Busetto, L., Chelle, M., Ceccherini, G., et al. (2015). The fourth phase of the radiative transfer model intercomparison (rami) exercise: Actual canopy scenarios and conformity testing. *Remote Sensing of Environment*, 169:418–437.

Xu, S., Zhou, K., Sun, Y., and Yun, T. (2021). Separation of wood and foliage for trees from ground point clouds using a novel least-cost path model. *IEEE Journal of Selected Topics in Applied Earth Observations and Remote Sensing*, 14:6414–6425.

Yamashita, M. and Yoshimura, M. (2019). Estimation of global and diffuse photosynthetic photon flux density under various sky conditions using ground-based whole-sky images. *Remote Sensing*, 11(8):932.



# Appendix A

**Table A1:** Per-sensor Pearson's correlation coefficient  $r$  for measured vs simulated values (Logger 1 and 2)

Logger	Sensor	Explicit Geometries	0.2 m Voxels	1 m Voxels
1	1	0.63	0.63	0.63
	2	0.50	-0.04	0.60
	3	0.20	-0.36	-0.12
	4	0.45	0.14	0.03
	5	0.90	0.62	0.78
	6	0.48	0.39	0.77
	7	-0.22	0.40	-0.02
	8	0.18	0.28	0.09
	9	0.33	0.80	0.84
	10	0.26	0.15	0.56
	11	0.44	0.05	0.25
	12	0.46	-0.12	0.15
2	1	0.99	0.98	1.00
	2	1.00	0.98	1.00
	3	0.99	0.48	0.38
	4	0.55	0.20	0.12
	5	0.99	0.99	1.00
	6	0.99	0.98	1.00
	7	0.73	0.44	0.37
	8	0.53	0.06	0.01
	9	0.99	0.99	1.00
	10	0.99	0.98	1.00
	11	0.68	0.47	0.36
	12	0.66	-0.01	-0.01

**Table A2:** Per-sensor Pearson’s correlation coefficient  $r$  for measured vs simulated values (Logger 3 and 4)

Logger	Sensor	Explicit Geometries	0.2 m Voxels	1 m Voxels
3	1	0.90	0.86	0.98
	2	0.70	0.52	0.84
	3	0.54	0.51	0.52
	4	0.51	0.30	0.00
	5	0.88	0.66	0.98
	6	0.20	0.07	0.34
	7	0.53	0.59	0.47
	8	0.80	0.70	0.66
	9	0.82	0.80	0.92
	10	0.80	0.79	0.77
	11	0.62	0.67	0.56
	12	0.96	0.82	0.76
4	1	0.99	0.99	1.00
	2	0.96	0.68	0.68
	3	0.64	0.72	0.69
	4	0.84	0.69	0.64
	5	0.75	0.75	0.75
	6	0.55	0.67	0.68
	7	0.80	0.58	0.64
	8	0.79	0.83	0.82
	9	1.00	0.99	1.00
	10	0.68	0.71	0.73
	11	0.64	0.45	0.34
	12	0.81	0.24	0.12

**Table A3:** Per-sensor Pearson’s correlation coefficient  $r$  for measured vs simulated values (Logger 5 and 6)

Logger	Sensor	Explicit Geometries	0.2 m Voxels	1 m Voxels
5	1	0.92	0.88	0.86
	2	0.97	0.89	0.79
	3	0.89	0.95	0.83
	4	0.94	0.83	0.74
	5	0.75	0.85	0.86
	6	0.90	0.90	0.87
	7	0.94	0.86	0.80
	8	0.83	0.79	0.64
	9	0.77	0.72	0.75
	10	0.86	0.66	0.75
	11	0.84	0.75	0.79
	12	0.87	0.71	0.64
6	1	0.93	0.82	0.79
	2	0.98	0.83	0.85
	3	0.98	0.86	0.89
	4	1.00	0.77	0.77
	5	0.93	0.71	0.77
	6	0.90	0.94	0.83
	7	0.66	0.59	0.41
	8	0.37	0.77	0.49
	9	0.93	0.88	0.90
	10	0.79	0.95	0.84
	11	0.84	0.66	0.57
	12	-0.30	-0.24	-0.36



## Appendix B

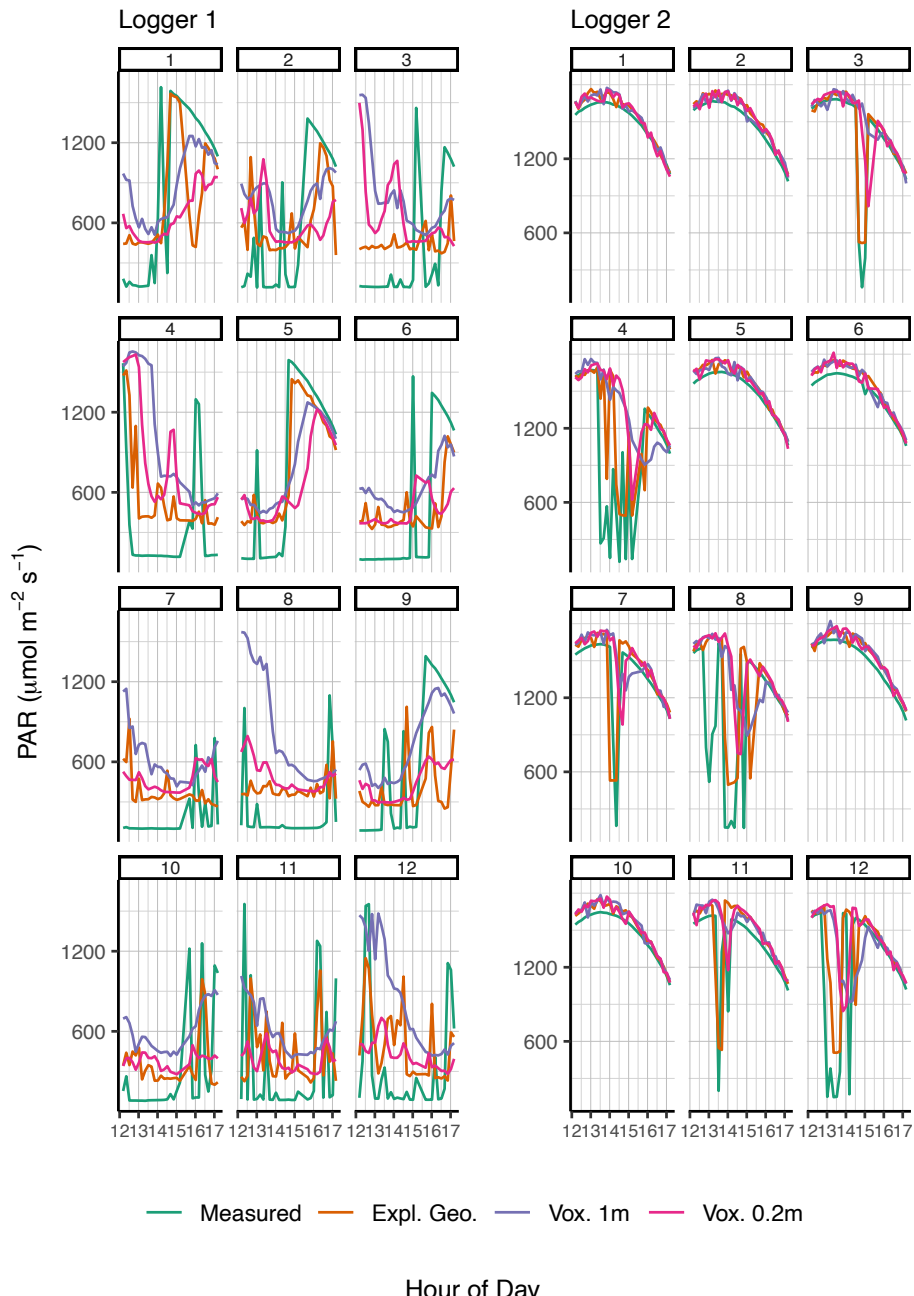


**Figure B1:** Time series of measured and simulated PAR values for all three scene types. (Logger 1, Logger 2)

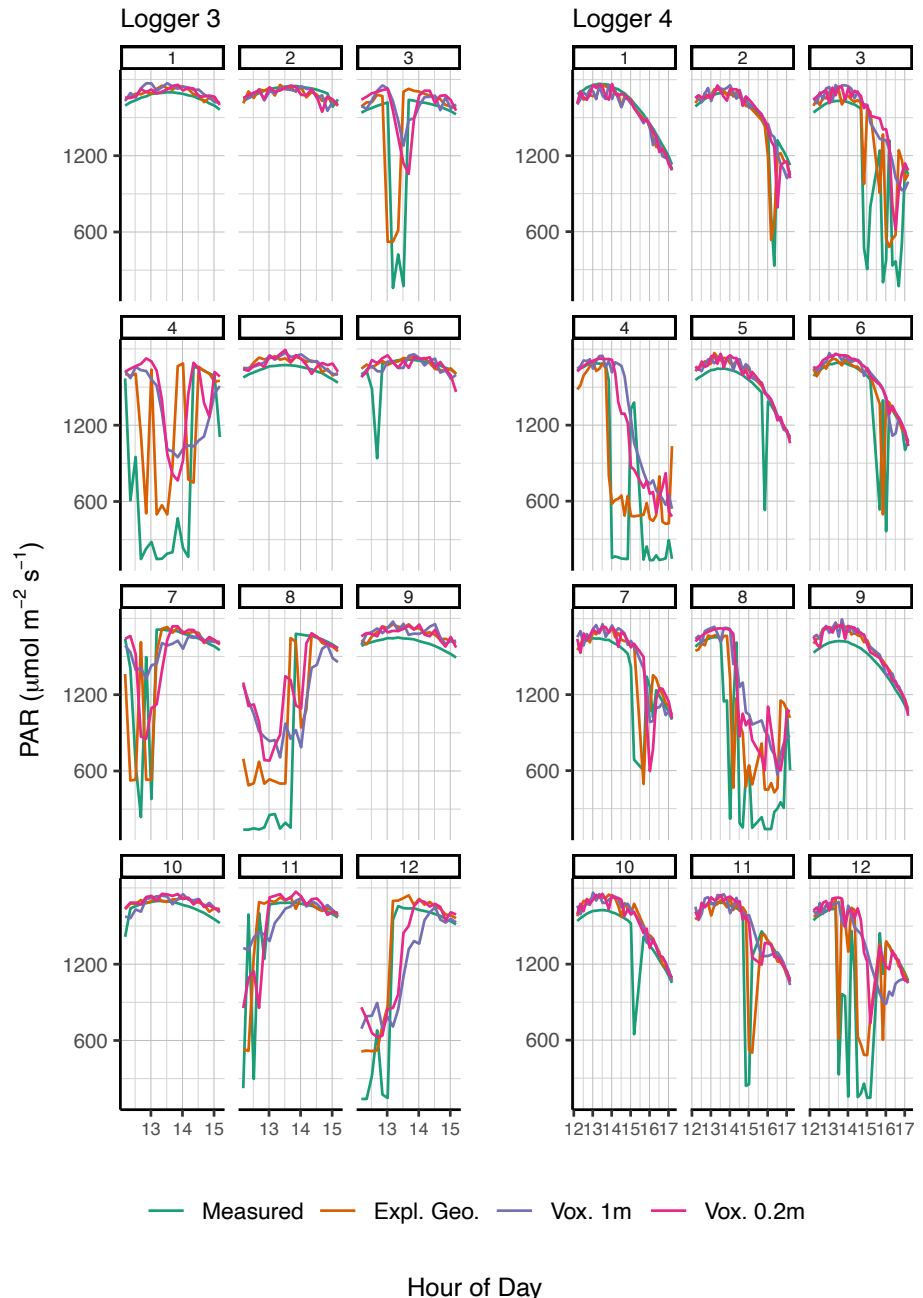


**Figure B2:** Time series of measured and simulated PAR values for all three scene types. (Logger 3, Logger 4)

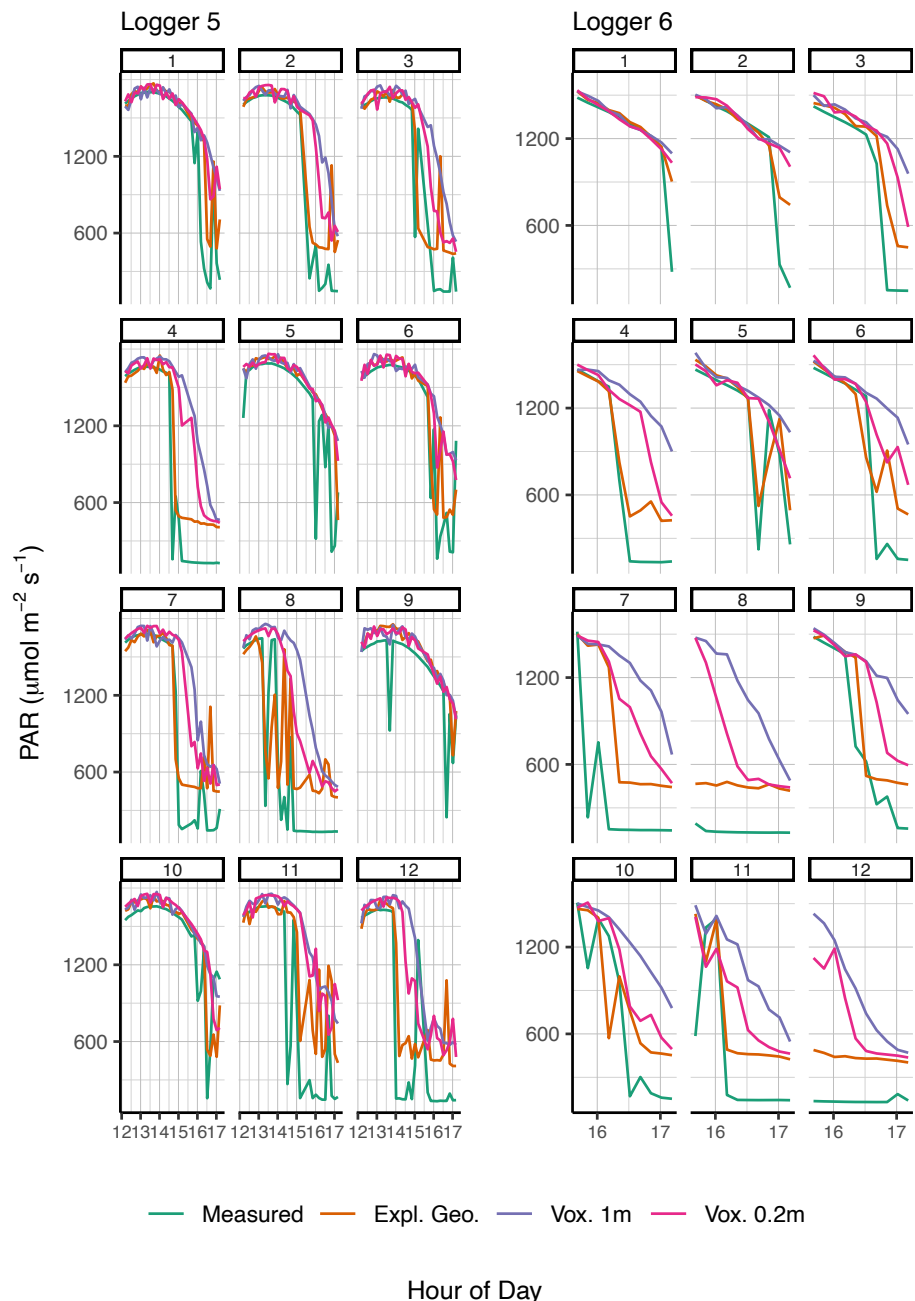


**Figure B3:** Time series of measured and simulated PAR values for all three scene types. (Logger 5, Logger 6)



## Eidesstattliche Erklärung\*

Hiermit erkläre ich,

McClatchy, Patrick  
Name, Vorname

20.11.1996  
Geburtsdatum

4547533  
Matrikelnummer

an Eides statt, dass ich die/das vorliegende(s) Hausarbeit/Essay/Abschlussarbeit\*\* mit dem Titel:

Advancing Forest Radiative Transfer Modeling: TLS-Derived Explicit Geometries in DART

selbstständig verfasst, ganz oder in Teilen noch nicht als Prüfungs- oder Studienleistung vorgelegt und keine anderen als die angegebenen Hilfsmittel benutzt habe. Sämtliche Stellen der Arbeit, die benutzten Werken im Wortlaut oder dem Sinn nach entnommen sind, habe ich durch Quellenangaben kenntlich gemacht. Dies gilt auch für Zeichnungen, Skizzen, bildliche Darstellungen und dergleichen sowie für Quellen aus dem Internet.

Mit meiner Unterschrift willige ich ein, dass meine Arbeit mittels einer Plagiatsssoftware überprüft werden kann und dass zu diesem Zweck elektronische Kopien (in anonymisierter Version) gefertigt und gespeichert werden können.

Freiburg, 01.07.2023 .....  
(Datum) .....  
(Unterschrift)

\* Diese Erklärung ist der eigenständig erstellten Arbeit als Anhang beizufügen. Arbeiten ohne diese Erklärung werden nicht angenommen. Auf die strafrechtliche Relevanz einer falschen Eidesstattlichen Erklärung wird hiermit hingewiesen.

\*\* nicht zutreffendes durchstreichen